

2017

The development of carbon nanomaterials enhanced potassium sensor and glucose sensor for applications in wearable sweat-based sensing

Qing He

Iowa State University

Follow this and additional works at: <https://lib.dr.iastate.edu/etd>



Part of the [Mechanical Engineering Commons](#)

Recommended Citation

He, Qing, "The development of carbon nanomaterials enhanced potassium sensor and glucose sensor for applications in wearable sweat-based sensing" (2017). *Graduate Theses and Dissertations*. 16101.

<https://lib.dr.iastate.edu/etd/16101>

This Thesis is brought to you for free and open access by the Iowa State University Capstones, Theses and Dissertations at Iowa State University Digital Repository. It has been accepted for inclusion in Graduate Theses and Dissertations by an authorized administrator of Iowa State University Digital Repository. For more information, please contact digirep@iastate.edu.

The development of carbon nanomaterials enhanced potassium sensor and glucose sensor for applications in wearable sweat-based sensing

by

Qing He

A thesis submitted to the graduate faculty
in partial fulfillment of the requirements for the degree of

MASTER OF SCIENCE

Major: Mechanical Engineering

Program of Study Committee:
Jonathan C. Claussen, Major Professor
Meng Lu
Stuart J. Birrell

Iowa State University

Ames, Iowa

2017

Copyright © Qing He, 2017. All rights reserved.

TABLE OF CONTENTS

	Page
ABSTRACT.....	iv
CHAPTER 1 INTRODUCTION	1
References	5
CHAPTER 2 INKJET PRINTED GRAPEHNE ELECTRODE WITH THERMAL ANNEALING.....	8
Methodology.....	8
Graphene electrode fabrication.....	9
Reference	10
CHAPTER 3 ION SELECTIVE SENSOR CHARACTERIZATION	12
Background and theory.....	12
Traditional liquid junction ion selective electrode.....	14
All solid state ion-selective electrodes.....	15
ISE characteristics.....	17
Linear sensing range and response slope	17
Detection limit	18
Response time	19
Selectivity	20
Stability and reproducibility	21
References	23
CHAPTER 4 ENABLING INKJET PRINTED GRAPHENE FOR ION SELECTIVE ELECTRODES WITH POST-PRINT THERMAL ANNEALING....	25
Introduction	25
Experimental section	26
Results and discussion	30
Conclusions	42
References	44
CHAPTER 5 SUMMARY AND CONCLUSIONS	47
References	49

ACKNOWLEDGMENTS

I would like to thank my major professor, Dr. Jonathan C. Claussen, and my committee members, Dr. Stuart J. Birrell and Dr. Meng Lu, for their guidance and support through the course of research. I am grateful for the opportunity to contribute such interesting research. Thanks for Dr. Jonathan C. Claussen's help and support through my graduate study.

Thanks for my friends and lab mates Suprem Das, Shaowei Ding, Allison Cargill, Nate Garland, Bolin Chen, John Hondred, Kshama Parate, and Loreen Stromberg who have encouraged me and assisted in the research during my graduate study.

In addition, I would like to thank my family for their love and support through all those years. Thanks for my parents who are the constant source of love and support. Thanks for my cousins, aunt and uncle for giving me encouragement and advices through this endeavor. I would like to express my heart-felt gratitude to my family.

ABSTRACT

Inkjet printed graphene (IPG) has recently shown tremendous promise in reducing the cost and complexity of graphene circuit fabrication. In this work, we fabricate an ion selective electrode (ISE) with IPG for the first time. A thermal annealing process in a nitrogen ambient environment converts the IPG into a highly conductive electrode (sheet resistance changes from $52.8 \pm 7.4 \text{ M}\Omega/\square$ for unannealed graphene to $172.7 \pm 33.3\Omega/\square$ for graphene annealed at 950°C). Raman spectroscopy and field emission scanning electron microscopy (FESEM) analysis reveals that the printed graphene flakes begin to smooth at an annealing temperature of 500°C and then become more porous and more electrically conductive when annealed at temperatures of 650°C and above. The resultant thermally annealed, IPG electrodes are converted into potassium ISEs via functionalization with a polyvinyl chloride (PVC) membrane and valinomycin ionophore. The developed potassium ISE displays a wide linear sensing range (0.01mM to 100mM), a low detection limit ($7 \mu\text{M}$), minimal drift ($8.6 \times 10^{-6} \text{ V/s}$), and a negligible interference during electrochemical potassium sensing against the backdrop of interfering ions [i.e., sodium (Na), magnesium (Mg), and calcium (Ca)] and artificial eccrine perspiration. Thus, the IPG ISE shows potential for potassium detection in a wide variety of human fluids including plasma, serum, and sweat.

CHAPTER 1

INTRODUCTION

Optical, piezoelectric and electrochemical based sensors have been widely used for detecting analytes in a wide variety of fluids¹. Electrochemical sensing is a low cost and rapid sensing modality that is conducive to in field sensing or point-of-care sensing applications.² Hand-held electrochemical sensors have long since been developed and commercialized for blood glucose monitoring³. However, the intrusive sample collecting methods of blood which includes pricking the finger with a lancet has impeded some patients from properly and consistently monitoring their blood glucose levels.³⁻⁴ Wearable sensors have drawn considerable attention owing to their non-invasive nature and the capability of continuous monitoring of patients' biological information.⁵⁻⁷ Recent research has shown promise in developing wearable sweat sensors for fluid analyte monitoring including analyzing electrolyte such as sodium⁸, chloride⁹, interleukin-6¹⁰, cortisol¹¹. Such sweat-based biosensors could be used to improve athletes' training efficiency by monitoring hydration and fatigue levels. Moreover, continuous sweat monitoring could provide valuable personalized information which would allow individuals to change their lifestyle and maintain an optimal health status. However, unlike well-developed wearable physical sensors like strain sensors¹², heart rate sensors¹³ and motion sensors¹⁴⁻¹⁵, biochemical analysis of sweat is still in its infancy and only limited commercialized wearable sweat sensors are available.

Indeed, wearable chemical sensors have been developed for monitoring fluid analytes in tears¹⁶, saliva¹⁷, and sweat¹⁸. Among these sensors, electrochemical sensors are perhaps the most promising due to their ability to continuously monitor and quantify concentrations of target analyte even in turbid solutions¹⁹⁻²¹. Furthermore, human sweat can provide plentiful health status

information²². For example, abnormal sodium, lactate, ammonium, and/or calcium levels in sweat can indicate electrolyte imbalance¹⁸, cystic fibrosis²³, physical stress²⁴, osteoporosis²⁵ and bone mineral loss²⁶. Continuous monitoring of these biological target levels can help patients obtain physiological balance. However, continuous monitoring of sweat analytes requires the sensors to be small in size, lightweight and mechanically flexible²⁷. Consequently, the challenges of properly designing and fabricating biosensors without comprising their electronic and electroactivity functionalities have impeded their implementation. Moreover, the fabrication of high resolution metal circuits is challenging and typically entails the development of meandering thin metal films on flexible substrates fabricated with cleanroom technology²⁸. Such techniques and devices are costly and hence not appropriate for sweat sensors that need to be regularly replaced/disposed as the biorecognition agent denatures the sensor sensitivity diminishes. Hence, a low-cost, alternative to creating flexible electrical circuits with thin metal films is needed. One solution to this conundrum is the use of printed carbon nanomaterials as the electrochemical, biosensor transduction element in lieu of metal circuits.²⁹⁻³¹

Printing technologies such as gravure and inkjet printing are providing revolutionary methods to manufacture cost-effective flexible sensors and electronics³²⁻³³. Compared to traditional labor extensive photolithography, printing technologies eliminate the need for photomasks or stencils and do not waste materials such as in spin coating. Consequently, the printing technologies are well-suited for economical, scalable manufacturing of electronics on flexible surfaces and larger surfaces (e.g., sheets of polymers from roll-to-roll manufacturing equipment)³⁴⁻³⁵. Recent research has helped shown the promise of using printed nanomaterials in diverse applications including pressure sensors³⁶⁻³⁷, radio frequency identification tags (RFID)³⁸⁻³⁹, solar cells⁴⁰, light emitting diodes (LED)⁴¹ and transistors⁴², chemical sensors⁴³, etc.

The contact printing methods such as gravure printing, gravure-offset printing, flexographic printing, micro-contact printing and roll to roll printing involve making pre-patterned molds that contact the substrate during the printing^{41, 44-47}. Each new pattern needs new pre-patterned parts which makes it costly to change the pattern. Unlike traditional contact printing, non-contact printing (e.g., inkjet printing, dispense printing) deposits solutions via openings/nozzles from cartridges or syringes that are rastered across a surface in a programmed manner. The inkjet printing techniques have attracted much attention because of the simple fabrication processes, high speed, lower material wastage rate, and high resolution (~50 μm).^{35, 48-51} ..

The conducting materials are the core functional component of printed electronics. Multiple conducting materials have been developed as inkjet printable ink, such as metal particles⁴⁹, crystalline organic conducting materials⁵², conducting polymers⁵³ and carbon nanomaterials⁵⁴⁻⁵⁵. Due to its remarkable electron mobility at room temperature, high flexibility, and high tensile strength and Young's modulus and inkjet printed is being researched for potential use in flexible electronics or for use as a replacement for ITO^{33, 49, 53}. Compared to the traditional graphene grown through chemical vapor deposition, inkjet printed graphene flakes provides a cost effective and simplified route to graphene circuit design. Furthermore, the graphene being inkjet printed could be rapidly produced in large batches via low cost solvent-exfoliation processes.³¹

Herein we demonstrate a solid-state ion selective sensor on thermally annealed, inkjet printed graphene. The developed ISE displays a wide linear sensing range, low detection limit minimal drift, and selectivity comparable with other potassium ISE sensor. These results are discussed in the following sections of this manuscript. Also, the data and writing from our

manuscript titled “Enabling Inkjet Printed Graphene for Ion Selective Electrodes with Postprint Thermal Annealing” published in the journal of ACS Applied Materials & Interfaces is used throughout the remaining portions of this thesis.

References

1. Turner, A., Biosensors: then and now. *Trends in biotechnology* **2013**, *31* (3), 119.
2. Ronkainen, N. J.; Halsall, H. B.; Heineman, W. R., Electrochemical biosensors. *Chemical Society Reviews* **2010**, *39* (5), 1747-1763.
3. Wang, J., Electrochemical biosensors: towards point-of-care cancer diagnostics. *Biosensors and Bioelectronics* **2006**, *21* (10), 1887-1892.
4. Zelin, M.; Jamieson, D., Reusable test unit for simulating electrochemical sensor signals for quality assurance of portable blood analyzer instruments. Google Patents: **1992**.
5. Windmiller, J. R.; Wang, J., Wearable electrochemical sensors and biosensors: a review. *Electroanalysis* **2013**, *25* (1), 29-46.
6. Kim, D.-H.; Lu, N.; Ghaffari, R.; Rogers, J. A., Inorganic semiconductor nanomaterials for flexible and stretchable bio-integrated electronics. *NPG Asia Materials* **2012**, *4* (4), e15.
7. Hammock, M. L.; Chortos, A.; Tee, B. C. K.; Tok, J. B. H.; Bao, Z., 25th anniversary article: the evolution of electronic skin (e-skin): a brief history, design considerations, and recent progress. *Advanced Materials* **2013**, *25* (42), 5997-6038.
8. Rose, D. P.; Ratterman, M. E.; Griffin, D. K.; Hou, L.; Kelley-Loughnane, N.; Naik, R. R.; Hagen, J. A.; Papautsky, I.; Heikenfeld, J. C., Adhesive RFID sensor patch for monitoring of sweat electrolytes. *IEEE Transactions on Biomedical Engineering* **2015**, *62* (6), 1457-1465.
9. Choi, D.-H.; Kim, J. S.; Cutting, G. R.; Searson, P. C., Wearable Potentiometric Chloride Sweat Sensor: The Critical Role of the Salt Bridge. *Analytical Chemistry* **2016**, *88* (24), 12241-12247.
10. Kumar, L. S.; Wang, X.; Hagen, J.; Naik, R.; Papautsky, I.; Heikenfeld, J., Label free nano-apptasensor for interleukin-6 in protein-dilute bio fluids such as sweat. *Analytical Methods* **2016**, *8* (17), 3440-3444.
11. Ventura, S. A.; Heikenfeld, J.; Brooks, T.; Esfandiari, L.; Boyce, S.; Park, Y.; Kasting, G. B., Cortisol extraction through human skin by reverse iontophoresis. *Bioelectrochemistry* **2017**, *114*, 54-60.
12. Yamada, T.; Hayamizu, Y.; Yamamoto, Y.; Yomogida, Y.; Izadi-Najafabadi, A.; Futaba, D. N.; Hata, K., A stretchable carbon nanotube strain sensor for human-motion detection. *Nature nanotechnology* **2011**, *6* (5), 296-301.
13. Tapia, E. M.; Intille, S. S.; Haskell, W.; Larson, K.; Wright, J.; King, A.; Friedman, R. In *Real-time recognition of physical activities and their intensities using wireless accelerometers and a heart rate monitor*, Wearable Computers, 2007 11th IEEE International Symposium on, IEEE: **2007**; pp 37-40.
14. Yang, C.-C.; Hsu, Y.-L., A review of accelerometry-based wearable motion detectors for physical activity monitoring. *Sensors* **2010**, *10* (8), 7772-7788.
15. Yang, A. Y.; Jafari, R.; Sastry, S. S.; Bajcsy, R., Distributed recognition of human actions using wearable motion sensor networks. *Journal of Ambient Intelligence and Smart Environments* **2009**, *1* (2), 103-115.
16. Bhandodkar, A. J.; Wang, J., Non-invasive wearable electrochemical sensors: a review. *Trends in biotechnology* **2014**, *32* (7), 363-371.
17. Vasudev, A.; Kaushik, A.; Tomizawa, Y.; Norena, N.; Bhansali, S., An LTCC-based microfluidic system for label-free, electrochemical detection of cortisol. *Sensors and Actuators B: Chemical* **2013**, *182*, 139-146.
18. Bergeron, M. F., Heat cramps: fluid and electrolyte challenges during tennis in the heat. *Journal of science and medicine in sport* **2003**, *6* (1), 19-27.
19. Biran, I.; Babai, R.; Levkov, K.; Rishpon, J.; Ron, E. Z., Online and in situ monitoring of environmental pollutants: electrochemical biosensing of cadmium. *Environmental Microbiology* **2000**, *2* (3), 285-290.
20. Turner, A. P., Biosensors: sense and sensibility. *Chemical Society Reviews* **2013**, *42* (8), 3184-3196.

21. Shah, J.; Wilkins, E., Electrochemical biosensors for detection of biological warfare agents. *Electroanalysis* **2003**, *15* (3), 157-167.
22. Mitsubayashi, K.; Suzuki, M.; Tamiya, E.; Karube, I., Analysis of metabolites in sweat as a measure of physical condition. *Analytica chimica acta* **1994**, *289* (1), 27-34.
23. Stern, R. C., The diagnosis of cystic fibrosis. *New England Journal of Medicine* **1997**, *336* (7), 487-491.
24. Pilardeau, P.; Vaysse, J.; Garnier, M.; Joublin, M.; Valeri, L., Secretion of eccrine sweat glands during exercise. *British journal of sports medicine* **1979**, *13* (3), 118.
25. Heaney, R. P., Calcium in the prevention and treatment of osteoporosis. *Journal of internal medicine* **1992**, *231* (2), 169-180.
26. Klesges, R. C.; Ward, K. D.; Shelton, M. L.; Applegate, W. B.; Cantler, E. D.; Palmieri, G. M.; Harmon, K.; Davis, J., Changes in bone mineral content in male athletes: mechanisms of action and intervention effects. *Jama* **1996**, *276* (3), 226-230.
27. Sekitani, T.; Noguchi, Y.; Hata, K.; Fukushima, T.; Aida, T.; Someya, T., A rubberlike stretchable active matrix using elastic conductors. *Science* **2008**, *321* (5895), 1468-1472.
28. Jin, X.; Jiang, C.; Song, E.; Fang, H.; Rogers, J. A.; Alam, M. A., Stability of MOSFET-Based Electronic Components in Wearable and Implantable Systems. *IEEE Transactions on Electron Devices* **2017**.
29. Das, S. R.; Nian, Q.; Cargill, A. A.; Hondred, J. A.; Ding, S.; Saei, M.; Cheng, G. J.; Claussen, J. C., 3D Nanostructured Inkjet Printed Graphene via UV-Pulsed Laser Irradiation Enables Paper-Based Electronics and Electrochemical Devices. *Nanoscale* **2016**, *8* (35), 15870-15879.
30. Chen, B.; Das, S. R.; Zheng, W.; Zhu, B.; Xu, B.; Hong, S.; Sun, C.; Wang, X.; Wu, Y.; Claussen, J. C., Inkjet Printing of Single-Crystalline Bi₂Te₃ Thermoelectric Nanowire Networks. *Advanced Electronic Materials* **2017**, *3* (4).
31. He, Q.; Das, S. R.; Garland, N. T.; Jing, D.; Hondred, J. A.; Cargill, A. A.; Ding, S.; Karunakaran, C.; Claussen, J. C., Enabling Inkjet Printed Graphene for Ion Selective Electrodes with Post-Print Thermal Annealing. *ACS Applied Materials & Interfaces* **2017**.
32. Katz, H. E., Recent advances in semiconductor performance and printing processes for organic transistor-based electronics. *Chemistry of Materials* **2004**, *16* (23), 4748-4756.
33. Perelaer, J.; Smith, P. J.; Mager, D.; Soltman, D.; Volkman, S. K.; Subramanian, V.; Korvink, J. G.; Schubert, U. S., Printed electronics: the challenges involved in printing devices, interconnects, and contacts based on inorganic materials. *Journal of Materials Chemistry* **2010**, *20* (39), 8446-8453.
34. Nathan, A.; Ahnood, A.; Cole, M. T.; Lee, S.; Suzuki, Y.; Hiralal, P.; Bonaccorso, F.; Hasan, T.; Garcia-Gancedo, L.; Dyadyusha, A., Flexible electronics: the next ubiquitous platform. *Proceedings of the IEEE* **2012**, *100* (Special Centennial Issue), 1486-1517.
35. Pease, R. F.; Chou, S. Y., Lithography and other patterning techniques for future electronics. *Proceedings of the IEEE* **2008**, *96* (2), 248-270.
36. Khan, S.; Tinku, S.; Lorenzelli, L.; Dahiya, R. S., Flexible tactile sensors using screen-printed P (VDF-TrFE) and MWCNT/PDMS composites. *IEEE sensors Journal* **2015**, *15* (6), 3146-3155.
37. Khan, S.; Lorenzelli, L.; Dahiya, R. In *Screen printed flexible pressure sensors skin*, Advanced Semiconductor Manufacturing Conference (ASMC), 2014 25th Annual SEMI, IEEE: **2014**; pp 219-224.
38. Jung, M.; Kim, J.; Noh, J.; Lim, N.; Lim, C.; Lee, G.; Kim, J.; Kang, H.; Jung, K.; Leonard, A. D., All-printed and roll-to-roll-printable 13.56-MHz-operated 1-bit RF tag on plastic foils. *IEEE Transactions on Electron Devices* **2010**, *57* (3), 571-580.
39. Zheng, Y.; He, Z.; Gao, Y.; Liu, J., Direct desktop printed-circuits-on-paper flexible electronics. *Scientific reports* **2013**, *3*.
40. Krebs, F. C., Fabrication and processing of polymer solar cells: a review of printing and coating techniques. *Solar energy materials and solar cells* **2009**, *93* (4), 394-412.
41. Sandström, A.; Dam, H. F.; Krebs, F. C.; Edman, L., Ambient fabrication of flexible and large-area organic light-emitting devices using slot-die coating. *Nature communications* **2012**, *3*, 1002.

42. Kim, T.-i.; Hwan Jung, Y.; Chung, H.-J.; Jun Yu, K.; Ahmed, N.; Corcoran, C. J.; Suk Park, J.; Hun Jin, S.; Rogers, J. A., Deterministic assembly of releasable single crystal silicon-metal oxide field-effect devices formed from bulk wafers. *Applied Physics Letters* **2013**, *102* (18), 182104.
43. Zhang, S.; Jiang, Z.; Shi, J.; Wang, X.; Han, P.; Qian, W., An Efficient, Recyclable, and Stable Immobilized Biocatalyst Based on Bioinspired Microcapsules-in-Hydrogel Scaffolds. *ACS applied materials & interfaces* **2016**, *8* (38), 25152-25161.
44. Radha, B.; Lim, S. H.; Saifullah, M. S.; Kulkarni, G. U., Metal hierarchical patterning by direct nanoimprint lithography. *Scientific reports* **2013**, *3*, 1078.
45. Kaufmann, T.; Ravoo, B. J., Stamps, inks and substrates: polymers in microcontact printing. *Polymer Chemistry* **2010**, *1* (4), 371-387.
46. Deganello, D.; Cherry, J.; Gethin, D.; Claypole, T., Patterning of micro-scale conductive networks using reel-to-reel flexographic printing. *Thin Solid Films* **2010**, *518* (21), 6113-6116.
47. Kang, H. W.; Sung, H. J.; Lee, T.-M.; Kim, D.-S.; Kim, C.-J., Liquid transfer between two separating plates for micro-gravure-offset printing. *Journal of Micromechanics and microengineering* **2008**, *19* (1), 015025.
48. Søndergaard, R. R.; Hösel, M.; Krebs, F. C., Roll-to-Roll fabrication of large area functional organic materials. *Journal of Polymer Science Part B: Polymer Physics* **2013**, *51* (1), 16-34.
49. Tobjörk, D.; Österbacka, R., Paper electronics. *Advanced Materials* **2011**, *23* (17), 1935-1961.
50. Leenen, M. A.; Arning, V.; Thiem, H.; Steiger, J.; Anselmann, R., Printable electronics: flexibility for the future. *physica status solidi (a)* **2009**, *206* (4), 588-597.
51. Subramanian, V.; Chang, J. B.; de la Fuente Vornbrock, A.; Huang, D. C.; Jagannathan, L.; Liao, F.; Mattis, B.; Molesa, S.; Redinger, D. R.; Soltman, D. In *Printed electronics for low-cost electronic systems: Technology status and application development*, Solid-State Device Research Conference, 2008. ESSDERC 2008. 38th European, IEEE: **2008**; pp 17-24.
52. Chiang, C. K.; Fincher Jr, C.; Park, Y. W.; Heeger, A. J.; Shirakawa, H.; Louis, E. J.; Gau, S. C.; MacDiarmid, A. G., Electrical conductivity in doped polyacetylene. *Physical Review Letters* **1977**, *39* (17), 1098.
53. Choi, M.-C.; Kim, Y.; Ha, C.-S., Polymers for flexible displays: from material selection to device applications. *Progress in Polymer Science* **2008**, *33* (6), 581-630.
54. Baughman, R. H.; Zakhidov, A. A.; De Heer, W. A., Carbon nanotubes--the route toward applications. *science* **2002**, *297* (5582), 787-792.
55. Su, D. S.; Centi, G., A perspective on carbon materials for future energy application. *Journal of Energy Chemistry* **2013**, *22* (2), 151-173.

CHAPTER 2

INKJET PRINTED GRAPHENE ELECTRODE WITH THERMAL ANNEALING

Methodology

Inkjet printing is increasingly being used to fabricate flexible electronics on large area surfaces. Inkjet printing is adaptable, involves less steps compare to other printing methods, is easy to change patterns for mass manufacturing, and can control the amount of material that deposit on the substrate. Different inks have been developed. Typically metal nanoparticle dispersions cannot keep stable in DI water and ordinary organic solvenst¹⁻². Consequently, stabilizers are needed to chemically modify the particles and disperse them¹. However, the stabilizer usually degrades in a couple years, and the metal can oxidase after printing¹⁻². Graphene is a promising material for inkjet printable electronics due to its good electrical conductivity, stability, and dispersibility in organic solvents³⁻⁵. Moreover, inkjet printed graphene which is produced by liquid phase exfoliation provides a cost effective method for graphene processing,⁶unlike costly and complex conventional graphene processing methods that use chemical vapor deposition⁷, sublimation of Si atoms by heat treatment of silicon carbide⁸, or segregation from metal substrates.⁹

The proper ink and jetting properties are critically important to proper inkjet printing^{1, 10}. Factors such as ink viscosity, surface tension, density as well as nozzle diameter can affect the formatting of the liquid droplet¹⁰. The lack of properly dispersed molecules or nanoparticles in the ink can potentially cause issues as well. To improve the printing stability and eliminate agglomeration of particles within the nozzles, ink particles dispersed in the ink should be no larger

than 1/50 of the nozzle diameter¹¹. In our work, we used a 0.8 μm syringe filter to eliminate larger particles from the ink and to prevent nozzle clogging¹².

During the printing, the distance between the substrate and printing nozzles needs to be coordinated to ensure a homogenous and high resolution printed pattern. The distance from the substrate must be close to the substrate to eliminate the distribution from the environment and diversion of the drop ejection trace, while a substrate too close to the nozzles causes the secondary drops to scatter off due to the initial drop jetting pressure during the printing of the primary drop¹⁰.

The “coffee ring effect”¹³ is among the crucial phenomena affecting the uniformity of the inkjet printed patterns^{1, 13}. This phenomenon happens when ink droplet contains dispersed particles evaporates on a surface and leave a higher density of particles around the edge or perimeter of the droplet^{11, 14}. It is caused by the different evaporation rates between the edge and the center of the droplet. In other words, the ink solvent evaporates faster from the edge than the center, while the solvent that evaporates from the edge it be refilled by the solvent from the center^{1, 13}. To eliminate the “coffee ring effect”, the droplet’s geometry need to be “frozen” after it forms a homogenous film on the substrate¹. This can be accomplished by increasing the environmental temperature and using an ink solvent within a lower boiling point and heat of vaporization. Consequently, a mixture of 85% cyclohexane and 15% Terpineol was used as the solvent to disperse the graphene. And the substrate temperature was set as 50°C to accelerate the evaporation and “freeze” the droplets on the substrate during the printing.

Graphene electrode fabrication

In our work, graphene electrodes were fabricated via inkjet printing with a Dimatix Materials Printer (DMP 2800, Fujifilm)¹². Single layer graphene powder (ASC Material FN1P0005) was

mixed in solvent composite of 85% cyclohexanone (Sigma-Aldrich 398241) and 15% terpineol (Sigma-Aldrich T3407). After mixing, probe sonication for thirty minutes followed by bath sonication for several hours to disperse the graphene. The ink was filtered using a 0.8 μm syringe filter (GE Whatman), loaded into a 10 pL Dimatix printer cartridge, and printed on silicon wafers (Silicon Quest International). Sixty layers were printed with drop spacing of 20 μm , substrate temperature of 50°C, and cartridge temperature of 30°C. Electrodes were then thermally annealed under flowing nitrogen at six different temperatures, 200°C, 350°C, 500°C, 650°C, 800°C, and 950°C for 1 hour. Resistance measurements across the electrode after annealing at 950 °C were approximately 75 Ω .

References

1. Singh, M.; Haverinen, H. M.; Dhagat, P.; Jabbour, G. E., Inkjet printing—process and its applications. *Advanced materials* **2010**, *22* (6), 673-685.
2. Luechinger, N. A.; Athanassiou, E. K.; Stark, W. J., Graphene-stabilized copper nanoparticles as an air-stable substitute for silver and gold in low-cost ink-jet printable electronics. *Nanotechnology* **2008**, *19* (44), 445201.
3. Geim, A. K.; Novoselov, K. S., The Rise of Graphene. *Nat Mater* **2007**, *6* (3), 183-191.
4. Bonaccorso, F.; Sun, Z.; Hasan, T.; Ferrari, A., Graphene photonics and optoelectronics. *Nature photonics* **2010**, *4* (9), 611-622.
5. Sun, Z.; Hasan, T.; Torrisi, F.; Popa, D.; Privitera, G.; Wang, F.; Bonaccorso, F.; Basko, D. M.; Ferrari, A. C., Graphene mode-locked ultrafast laser. *ACS nano* **2010**, *4* (2), 803-810.
6. Hasan, T.; Torrisi, F.; Sun, Z.; Popa, D.; Nicolosi, V.; Privitera, G.; Bonaccorso, F.; Ferrari, A., Solution - phase exfoliation of graphite for ultrafast photonics. *physica status solidi (b)* **2010**, *247* (11 - 12), 2953-2957.
7. Reina, A.; Jia, X.; Ho, J.; Nezich, D.; Son, H.; Bulovic, V.; Dresselhaus, M. S.; Kong, J., Large area, few-layer graphene films on arbitrary substrates by chemical vapor deposition. *Nano letters* **2008**, *9* (1), 30-35.
8. Emtsev, K. V.; Bostwick, A.; Horn, K.; Jobst, J.; Kellogg, G. L.; Ley, L.; McChesney, J. L.; Ohta, T.; Reshanov, S. A.; Röhrl, J., Towards wafer-size graphene layers by atmospheric pressure graphitization of silicon carbide. *Nature materials* **2009**, *8* (3), 203-207.
9. Sutter, P. W.; Flege, J.-I.; Sutter, E. A., Epitaxial graphene on ruthenium. *Nature materials* **2008**, *7* (5), 406-411.
10. Derby, B.; Reis, N., Inkjet printing of highly loaded particulate suspensions. *MRS bulletin* **2003**, *28* (11), 815-818.
11. Van Osch, T. H.; Perelaer, J.; de Laat, A. W.; Schubert, U. S., Inkjet printing of narrow conductive tracks on untreated polymeric substrates. *Advanced Materials* **2008**, *20* (2), 343-345.

12. He, Q.; Das, S. R.; Garland, N. T.; Jing, D.; Hondred, J. A.; Cargill, A. A.; Ding, S.; Karunakaran, C.; Claussen, J. C., Enabling Inkjet Printed Graphene for Ion Selective Electrodes with Post-Print Thermal Annealing. *ACS Applied Materials & Interfaces* **2017**.
13. Deegan, R. D.; Bakajin, O.; Dupont, T. F.; Huber, G.; Nagel, S. R.; Witten, T. A., Capillary flow as the cause of ring stains from dried liquid drops. *Nature* **1997**, *389* (6653), 827-829.
14. de Gans, B. J.; Duineveld, P. C.; Schubert, U. S., Inkjet printing of polymers: state of the art and future developments. *Advanced materials* **2004**, *16* (3), 203-213.

CHAPTER 3

SOLID STATE ION SELECTIVE SENSOR CHARACTERIZATION

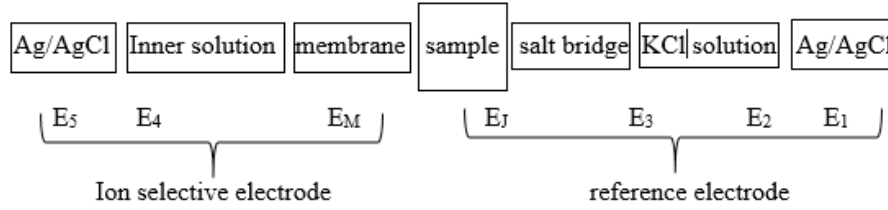
Background and theory

Solid state ion selective sensors show their potential to be wearable sensors for sweat pH^1 , ammonium², sodium³, potassium⁴⁻⁵, calcium⁶ sensing due to their simple fabrication and test method, wide sensing range, fast response, high sensitivity and small size.

Ion selective electrodes (ISEs) are electrochemical sensors with a thin ion selective membrane as the recognition element. The principal component of ISEs is the potential difference response, which is associated with permselective mass transfer of ions across a phase boundary. The selective membrane usually consists of a semi-permeable material which can control the ions passing through the membrane. The membrane separates the internal solution and the test solution and is responsible for the electromotive force (EMF) response and selectivity of the ISE.

The potential of the individual ion selective electrode cannot be measured. An ISE is as a half-cell that must be used in conjunction with a reference electrode to form a complete electrochemical cell. The working electrode and reference electrode are immersed into a solution to make a galvanic cell. The potential response of the working electrode obeys the Nernstian equation while the reference electrode keeps the potential constant. Consequently, the measured result is the electromotive force (EMF), which is the potential difference between the working electrode (ion selective electrode) and reference electrode (Ag/AgCl electrode).

The potential across the galvanic cell consists of a standard liquid junction ion selective electrode and a reference electrode with salt bridge can be considered as follows.



The EMF across the cell can be described by the equation shown below⁷.

$$EMF = (E_1 + E_2 + E_3 + E_4 + E_5) + E_M + E_J = E_{const} + E_M + E_J$$

Since E_1 to E_5 are sample independent, the EMF is actually determined by the membrane potential and liquid junction potential at the interface between the salt bridge and sample solution. The liquid junction potential can be considered as the sum of integrals of all charged ions in the diffusion layer at the salt bridge and saturated KCl solution. The liquid junction potential can be minimized by filling the salt bridge with concentrated electrolytes of similar nobilities. Or, the E_J can be estimated by the Henderson equation. Consequently, the potential EMF is mainly determined by the E_M and the E_M can be further explained by the following equation

$$E_M = E_{SM} + E_D + E_{MI} \quad (1)$$

E_{SM} represents the phase boundary potential at sample/membrane interface, E_D represents the diffusion potential in the membrane and E_{MI} is the membrane/inner filling solution interface phase boundary potential. Usually, E_{MI} is constant since it is independent of sample solution and E_D is zero. So it can be described as

$$E_M = E_{SM} + E_{const} \quad (2)$$

The E_{SM} can be derived from the basic thermodynamic theory. The electrochemical potential of target ion I in solution phase is⁸

$$\tilde{\mu}_I = \mu_I + z_I F \Phi \quad (3)$$

F is the Faraday constant, z_I is the ion charge, μ_I is the chemical potential and Φ is the electrical potential.

$$\mu_I = \mu_I^0 + RT \ln a_I \quad (4)$$

The μ_I^0 is the standard values of the chemical potential, R is the gas constant, and a_I is the activity of target ion I. T is the temperature in Kelvins. The activity of target ion can be correlated to the concentration of target ion I C_I through equation $a_I = \gamma_I C_I$. Consequently, the potential between membrane and solution φ_{SM} can be derived from the electrochemical potential difference between solution and membrane as the following equation.

$$\varphi_{SM} = \phi_M - \phi_S = \frac{\mu_I^M - \mu_I^S}{z_I F} = \frac{\mu_I^{0,M} - \mu_I^{0,S}}{z_I F} - \frac{RT}{z_I F} \ln \frac{a_I^M}{a_I^S} \quad (5)$$

To make $\frac{\mu_I^{0,M} - \mu_I^{0,S}}{z_I F} - \frac{RT}{z_I F} \ln a_I^M = \varphi^0$ The equation can be further simplified as below:

$$\varphi_{SM} = \varphi^0 + \frac{RT}{z_I F} \ln a_I^S \quad (6)$$

The equation shown above is the Nernst equation. The measured potential differences between ISE and reference electrode are linearly related to the logarithm of the target ion activity in solution.

Traditional liquid junction ion selective electrodes

Traditional liquid junction ion selective electrodes usually contain an internal solution or gel. The structure of the ion selective electrode is shown in Figure 1 a. In order to obtain a reproducible and stable electrical potential at the interface between the membrane and the internal solution, the internal solution contains an ion to which the membrane is selective. In this ISE system, the membrane and internal solution are responsible to conduct the ion from the test solution. An Ag/AgCl internal electrode is applied between the conductive wire and the internal solution in the working electrode to obtain the reversible transduction from the ionic conductivity

to the electronic conductivity. In a conventional ISE, charge transfer is realized by ion transfer across the membrane into the internal solution, charge is carried by ions in test solution and internal solution. Between the interface of internal solution and Ag/AgCl electrodes, reversible redox reaction happens between Ag atoms and Ag^+ cations which produce electrons. In this way, when all charge transfer processes are fast enough, no “blocking” between interfaces happens and the electrode is non-polarized.

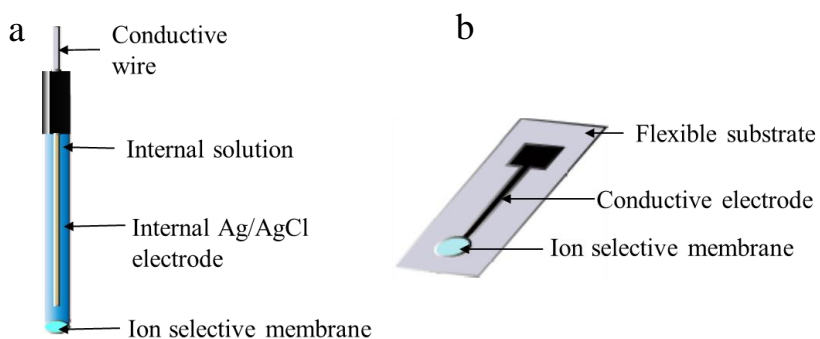


Figure 1. The diagram shows the structure of traditional liquid junction ion selective electrodes and solid state ion selective electrode.

All-solid-state ion-selective electrodes

Since it is difficult to minimize the traditional liquid junction ISEs, the solid state ISEs are developed which replace the inner Ag/AgCl reference electrode and inner electrolyte solution with an electronic conductor which is shown in figure 1 b. The electrodes are functionalized by directly depositing the ion selective membrane to the solid transducer layer of the electrode. The charge transfer is accomplished by both ionic and electronic conductivities. The solid-state ion selective electrode replaces the internal solution and internal reference electrode in the liquid junction ion selective electrode with a solid-state transducer layer.

The first all-solid-state ion selective electrode had been introduced as a coated wire electrode (CWE) which was functionalized by directly drop coating the ion selective membrane

on the metal wire electrode⁹. The CWEs show poor long-term reproducibility and stability. The instability was caused by the “blocking” between the metal wire and membrane interface. The “blocking” is attributed to the polarized electrode with a low transduction rate from ionic conductivity to electronic conductivity between the interface¹⁰. Therefore, materials such as hydrogels and conductive polymers have been explored as the transducer layers between the interface. Hydrogel materials as the transducer layers have shown smaller drifts than CWE sensors¹¹. However, the hydrogel based ISEs can't be considered as the true SC-ISE since the hydrogel shrink or swell when the environment humidity changes¹². Conductive polymers, such as poly(pyrrole) (PPy)¹³⁻¹⁴, poly(aniline)(PANI)¹⁵⁻¹⁶, poly(thiophene) (PT)¹⁷⁻¹⁹, poly(benzopyrene)²⁰, polyacrylate²¹, and their derivatives, have been commonly used as the transducer layers due to their suitable redox and ion exchange capabilities which lead to high stability of the ISE and minimized the polarizability of the solid contact. However, the polymer transducers sensitive to oxygen, CO₂, pH and light, which introduce interferences and decrease the shelf life of the electrodes²².

Carbon based materials have been investigated as the transduction layer on the ISE to improve the sensing performance. Graphite with surface-confined redox buffer systems have been used in SC-ISEs. Moreover, recently carbon based nanomaterials with high surface area such as, graphene, carbon nanotubes (CNTs)²³⁻²⁴, three dimensionally ordered macroporous carbon (3DOM carbon)²⁵⁻²⁶, and fullerenes²⁷, have been used as the transduction layer. These electrodes exhibited Nernstian slope, good selectivity, low detection limit, short response time and stability that are comparable to other SC-ISEs. Moreover, unlike their conductive polymer counterparts, these electrodes provide better stability for infield applications due to their insensitivity to the oxygen, CO₂, pH and light²⁸.

ISE characteristics

For practical use of ISEs, the sensing range, response slope, selectivity, response time, stability, and reproducibility of the electrodes are crucial indexes to estimate the sensing performance of electrodes. By spiking the DI water with the target ion, the potential response verses time, and, consequently, the calibration curve (potential verse logarithm of potassium ion concentration) could be obtained as shown in Figure 2.

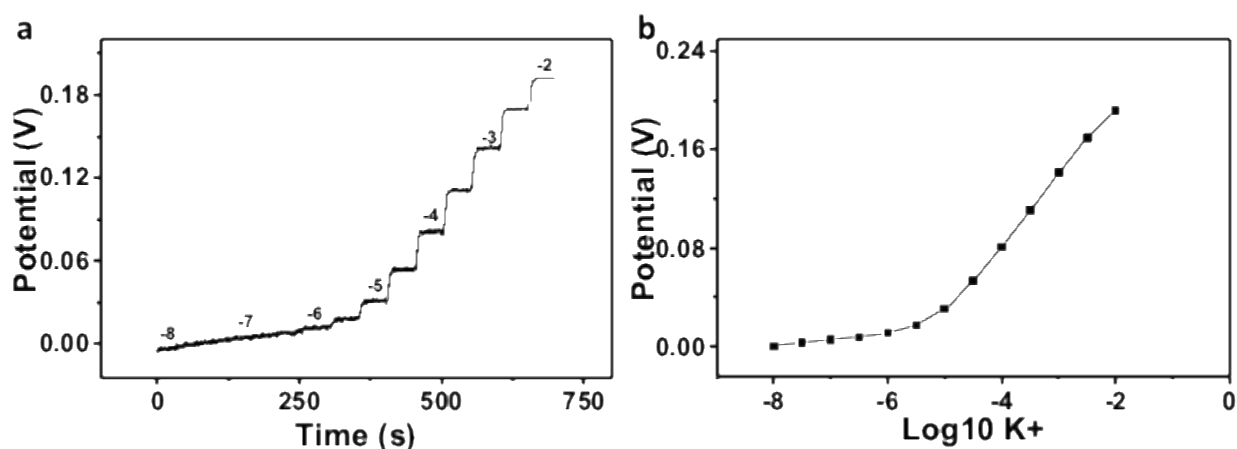


Figure 2. (a) Potential response of a potassium ISE verses time. Calibration curve of a ISE potential response verses logarithm potassium concentration of target ion.

Linear sensing range and response slope

The Linear sensing range and response slope can be obtained from the curve of the cell EMF verses the logarithm of the single ionic activity of a given species (calibration curve). As shown in figure 3, the linear sensing range is the linear part of the calibration curve. The response slope follows the Nerstain equatio as shown above.

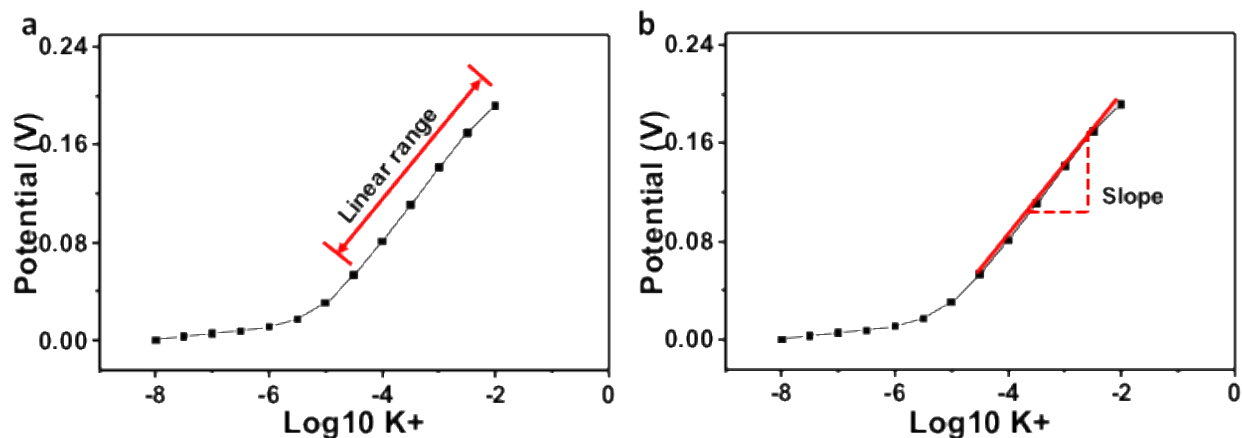


Figure 3. (a) The linear sensing range of the potassium ISE was shown in the calibration curve where the potential response linearly corresponds to the logarithm concentration of potassium concentration in the test solution. (b) The response slope is the slope of the linear sensing range which indicates the sensitivity of the sensor. The response slope obeys the Nernst equation, ideally, at 25 °C the response slope is 59.18mV/decade.

Detection limit

As shown in the figure 4, detection limit is taken as the intersection of final low concentration level segments (region 1) and the extrapolated linear range of the calibration curve (region 2).

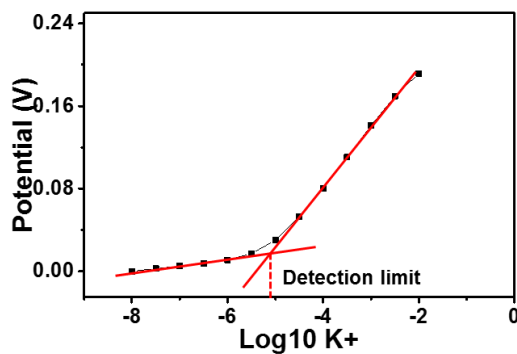


Figure 4. Detection limit that is determined from the calibration curve.

To ensure the reliability of the calculated detection limit, three measurements are required to provide the calibrating curve and calculate the detection limit. Last five data points in both low concentration level segment (region 1) and linear sensing segment (region 2) should be taken to determine the parameters. The determined detection limit should be provided with a standard deviation.

Response time

The response time of an ISE shows the time an ISE takes to reach the steady value of the EMF when the sample composite or concentration is changed. The characteristic is an important parameter to indicate the throughput of an ISE. The response time is defined as the time which is sufficient for 90% of the full potential changes. Figure 5 shows the determination of the response time.

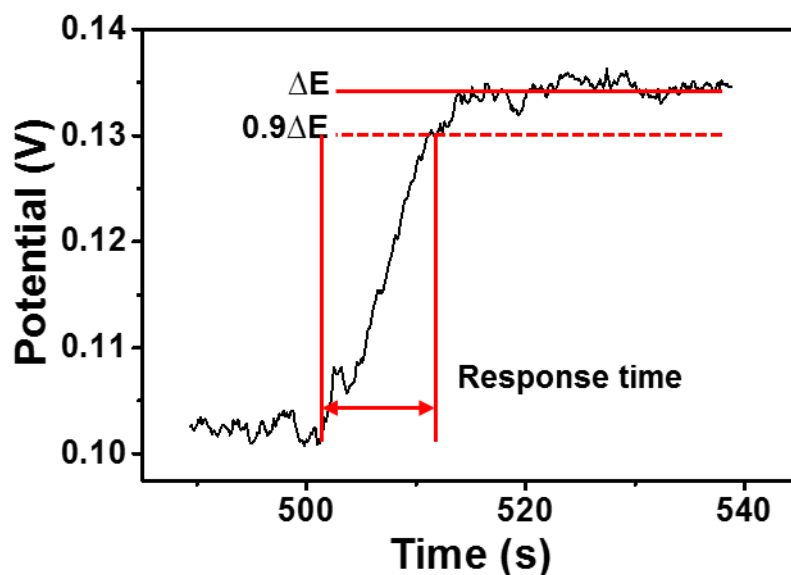


Figure 5. the response time is defined as the time from the target ion concentration begin to change to the sensor response reaches 90% of the full potential change.

Selectivity

The selectivity of an ISE is defined by the ability of electrode to distinguish the primary ion from other interference ions. The selectivity for each interference ion can be characterized with the thermodynamically founded selectivity coefficient $K_{I,J}^{pot}$. The selectivity coefficient $K_{I,J}^{pot}$ was originally derived from the empirical Nicolsky-Eisenman equation.

$$EMF = E_I^0 + (RT/z_I F) \ln(a_I + \sum K_{IJ}^{pot} a_J^{z_I/z_J}) \quad (7)$$

Where EMF the ion selective sensor' sensing response to the tested solution. E_I^0 is the initial potential of the sensor, R is the gas constant, F is the Faraday constant, and T is the temperature in Kelvins. And a_I is the activity of target ion I, a_J is the activity of target ion J, z_I is the ion I charge, z_J is the ion J charge.

Fixed interference method and separation solution method are commonly used to the obtain the selectivity coefficient $K_{I,J}^{pot}$ ²⁹. By using separation solution methods, the electrode's potential response to ion I and J are measured in 0.1 M solution I and J separately in our work⁵. Each method is schematically outlined in Figure 6 a. The obtained potential responses to ion I, E_I , and potential response to ion J, E_J , are used to calculate the selectivity coefficients based on the thermodynamically founded equation shown below. Then, the selectivity coefficient can be used to predict the response function in mixed samples.

$$K_{IJ}^{pot} = \exp[(E_J^0 - E_I^0)z_I F/RT] \quad (8)$$

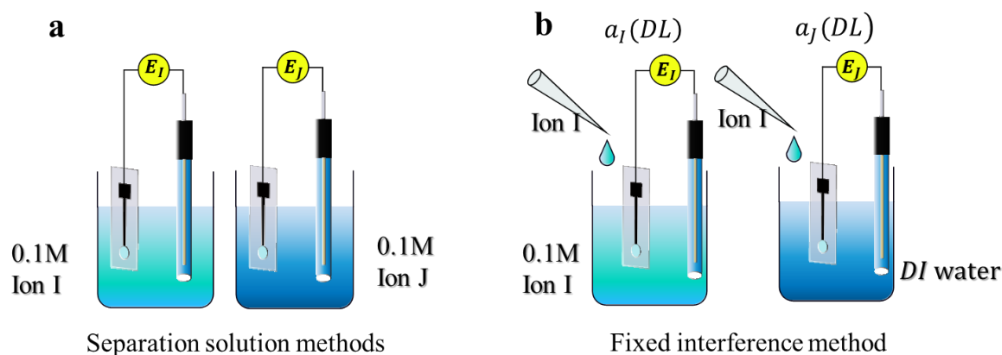


Figure 6. (a) Separation solution method to test the selectivity coefficient. In our work the ISE's potential responses in 0.1 M primary ion I and interference ion J are measured and the interference coefficient was calculated. (b) Fixed interference method to test the selectivity coefficient. The ISE's detection limits to primary ion in DI water and in 0.1M interference ion I are tested, and the selectivity coefficient can be calculated.

Fixed interference methods is also based on the determination of E_I and E_J from the measurement. The experiment steps are shown is Figure 6b. In practice, solution with constant concentration of an interference ion is spiked with primary ion until a Nernstian response to the primary ion is shown. By analysis the primary ion activity a_I at this detection limit ($a_I(DL)$) and the interfering ion activity in the background a_J ($a_J(DL)$), selectivity coefficient can be calculated by the equation listed below.

$$\log K_{IJ}^{pot} = \log a_I(DL)/a_J(DL)^{z_I/z_J} \quad (9)$$

Stability and reproducibility

Drift is the slow non-random change in EMF of an ISE over time in a solution with constant composition and temperature. Drift happens occurring over time indicates the initial potential or the sensing slope changes during the calibration. Drift hinders the converting of measured EMF to the ion concentration, which will put the reliability of the sensing result in question. The potential

stability of the SC-ISE is usually studied using constant-current chronopotentiometric measurements as noted by Bobacka¹⁷. In short, a constant current (e.g., 1nA) is applied to the electrode for a short time (e.g., 60s) and then a constant current of 1nA is applied to the electrode. The drift can be derived from the potential change during the time the constant current be applied.

References

1. Bandodkar, A. J.; Hung, V. W.; Jia, W.; Valdés-Ramírez, G.; Windmiller, J. R.; Martinez, A. G.; Ramírez, J.; Chan, G.; Kerman, K.; Wang, J., Tattoo-based potentiometric ion-selective sensors for epidermal pH monitoring. *Analyst* **2013**, *138* (1), 123-128.
2. Guinovart, T.; Bandodkar, A. J.; Windmiller, J. R.; Andrade, F. J.; Wang, J., A potentiometric tattoo sensor for monitoring ammonium in sweat. *Analyst* **2013**, *138* (22), 7031-7038.
3. Bandodkar, A. J.; Molinnus, D.; Mirza, O.; Guinovart, T.; Windmiller, J. R.; Valdés-Ramírez, G.; Andrade, F. J.; Schöning, M. J.; Wang, J., Epidermal tattoo potentiometric sodium sensors with wireless signal transduction for continuous non-invasive sweat monitoring. *Biosensors and bioelectronics* **2014**, *54*, 603-609.
4. Guinovart, T.; Parrilla, M.; Crespo, G. A.; Rius, F. X.; Andrade, F. J., Potentiometric Sensors Using Cotton Yarns, Carbon Nanotubes and Polymeric Membranes. *Analyst* **2013**, *138* (18), 5208-5215.
5. He, Q.; Das, S. R.; Garland, N. T.; Jing, D.; Hondred, J. A.; Cargill, A. A.; Ding, S.; Karunakaran, C.; Claussen, J. C., Enabling Inkjet Printed Graphene for Ion Selective Electrodes with Post-Print Thermal Annealing. *ACS Applied Materials & Interfaces* **2017**.
6. Bergeron, M. F., Heat cramps: fluid and electrolyte challenges during tennis in the heat. *Journal of science and medicine in sport* **2003**, *6* (1), 19-27.
7. Bakker, E.; Bühlmann, P.; Pretsch, E., Carrier-based ion-selective electrodes and bulk optodes. 1. General characteristics. *Chemical Reviews* **1997**, *97* (8), 3083-3132.
8. Mikhelson, K. N., *Ion-selective electrodes*. Springer: **2013**.
9. Cattrall, R.; Freiser, H., Coated wire ion-selective electrodes. *Analytical Chemistry* **1971**, *43* (13), 1905-1906.
10. Freiser, H., *Ion-selective electrodes in analytical chemistry*. Springer Science & Business Media: **2012**.
11. Cosofret, V. V.; Erdösy, M.; Johnson, T. A.; Buck, R. P.; Ash, R. B.; Neuman, M. R., Microfabricated sensor arrays sensitive to pH and K⁺ for ionic distribution measurements in the beating heart. *Analytical Chemistry* **1995**, *67* (10), 1647-1653.
12. Bobacka, J., Conducting Polymer - Based Solid - State Ion - Selective Electrodes. *Electroanalysis* **2006**, *18* (1), 7-18.
13. Cadogan, A.; Gao, Z.; Lewenstam, A.; Ivaska, A.; Diamond, D., All-solid-state sodium-selective electrode based on a calixarene ionophore in a poly (vinyl chloride) membrane with a polypyrrole solid contact. *ANALYTICAL CHEMISTRY-WASHINGTON DC* **1992**, *64*, 2496-2496.
14. Kisiel, A.; Mazur, M.; Kuśnieruk, S.; Kijewska, K.; Krysiński, P.; Michalska, A., Polypyrrole microcapsules as a transducer for ion-selective electrodes. *Electrochemistry Communications* **2010**, *12* (11), 1568-1571.
15. Evtugyn, G.; Belyakova, S.; Shamagsumova, R.; Saveliev, A.; Ivanov, A.; Stoikova, E.; Dolgova, N.; Stoikov, I.; Antipin, I.; Budnikov, H., Discrimination of apple juice and herbal liqueur brands with solid-state electrodes covered with polyaniline and thiacalixarenes. *Talanta* **2010**, *82* (2), 613-619.
16. Lindfors, T.; Szucs, J.; Sundfors, F.; Gyurcsanyi, R. E., Polyaniline nanoparticle-based solid-contact silicone rubber ion-selective electrodes for ultratrace measurements. *Analytical chemistry* **2010**, *82* (22), 9425-9432.
17. Bobacka, J., Potential Stability of All-Solid-State Ion-Selective Electrodes Using Conducting Polymers as Ion-To-Electron Transducers. *Anal. Chem.* **1999**, *71* (21), 4932-4937.
18. Chumbimuni-Torres, K. Y.; Rubinova, N.; Radu, A.; Kubota, L. T.; Bakker, E., Solid contact potentiometric sensors for trace level measurements. *Analytical chemistry* **2006**, *78* (4), 1318.
19. Bobacka, J.; McCarrick, M.; Lewenstam, A.; Ivaska, A., All solid-state poly (vinyl chloride) membrane ion-selective electrodes with poly (3-octylthiophene) solid internal contact. *Analyst* **1994**, *119* (9), 1985-1991.

20. Lisak, G.; Wagner, M.; Kvarnström, C.; Bobacka, J.; Ivaska, A.; Lewenstam, A., Electrochemical Behaviour of Poly (benzopyrene) Films Doped with Eriochrome Black T as a Pb²⁺ - Sensitive Sensors. *Electroanalysis* **2010**, *22* (23), 2794-2800.
21. Jaworska, E.; Kisiel, A.; Maksymiuk, K.; Michalska, A., Lowering the resistivity of polyacrylate ion-selective membranes by platinum nanoparticles addition. *Analytical chemistry* **2010**, *83* (1), 438-445.
22. Lindfors, T., Light sensitivity and potential stability of electrically conducting polymers commonly used in solid contact ion-selective electrodes. *Journal of Solid State Electrochemistry* **2009**, *13* (1), 77-89.
23. Düzgün, A.; Maroto, A.; Mairal, T.; O'Sullivan, C.; Rius, F. X., Solid-contact potentiometric aptasensor based on aptamer functionalized carbon nanotubes for the direct determination of proteins. *Analyst* **2010**, *135* (5), 1037-1041.
24. Hernández, R.; Riu, J.; Rius, F. X., Determination of calcium ion in sap using carbon nanotube-based ion-selective electrodes. *Analyst* **2010**, *135* (8), 1979-1985.
25. Fierke, M. A.; Lai, C.-Z.; Bühlmann, P.; Stein, A., Effects of architecture and surface chemistry of three-dimensionally ordered macroporous carbon solid contacts on performance of ion-selective electrodes. *Analytical chemistry* **2010**, *82* (2), 680.
26. Lai, C.-Z.; Fierke, M. A.; Stein, A.; Bühlmann, P., Ion-selective electrodes with three-dimensionally ordered macroporous carbon as the solid contact. *Analytical chemistry* **2007**, *79* (12), 4621-4626.
27. Fouskaki, M.; Chaniotakis, N., Fullerene-Based Electrochemical Buffer Layer for Ion-Selective Electrodes. *Analyst* **2008**, *133* (8), 1072-1075.
28. Crespo, G. A.; Macho, S.; Rius, F. X., Ion-Selective Electrodes Using Carbon Nanotubes as Ion-To-Electron Transducers. *Anal. Chem.* **2008**, *80* (4), 1316-1322.
29. Bakker, E.; Pretsch, E.; Bühlmann, P., Selectivity of potentiometric ion sensors. *Analytical chemistry* **2000**, *72* (6), 1127-1133.

CHAPTER 4

ENABLING INKJET PRINTED GRAPHENE FOR ION SELECTIVE ELECTRODES WITH POST-PRINT THERMAL ANNEALING
ENABLING INKJET PRINTED GRAPHENE FOR ION SELECTIVE ELECTRODES WITH POST-PRINT THERMAL ANNEALING

This thesis culminates in the results and discussion presented in this chapter. This chapter was published in the journal of ACS Applied Materials & Interfaces under the title “Enabling Inkjet Printed Graphene for Ion Selective Electrodes with Post-print Thermal Annealing”.

Introduction

The incorporation of both single-layer and multi-layer graphene into electrodes has significantly improved the sensitivity, detection limit, response time, and biocompatibility of electrochemical sensors and biosensors.¹⁻² The enhanced performance of graphene-based sensors/biosensors³⁻⁷ are attributed to the unique and advantageous material properties of graphene including high electron mobility of up to $200,000 \text{ cm}^2 \text{ V}^{-1} \text{ s}^{-1}$, high nominal surface area of $2630 \text{ m}^2 \text{ g}^{-1}$, and high tensile strength of 42 N m^{-1} as well as the relative ease or conduciveness to functionalize graphene with biorecognition agents. Furthermore, the electrochemical properties of graphene and other graphitic materials in general (e.g., highly ordered pyrolytic graphite (HOPG), graphene oxide (GO), carbon nanotubes (CNTs) and graphite) can be enhanced by inducing edge plane like-sites/defects and defect site functional groups onto the carbon surface through a variety of techniques (e.g., plasma etching, ion bombardment, and wet etching) to increase heterogeneous electron transfer rates and hence improve sensitivity/detection limits of electrochemical sensors.⁸⁻

¹² Additional graphene modification techniques such as nitrogen doping¹³⁻¹⁴ and metallic

nanoparticle integration¹⁵⁻¹⁶ have also been developed to improve graphene sensor performance. Indeed the use of graphene and ‘modified’ graphene have shown tremendous promise for electrochemical sensing, but the high cost and complexity of graphene electrode fabrication (fabrication that often requires lithographic patterning and high temperature chemical vapor deposition in a vacuum chamber reactor) and subsequent chemical modification steps has impeded their implementation and commercialization in a wide variety of in-field and point-of-care applications.¹⁷

IPG has recently shown tremendous promise in reducing the cost and complexity of graphene circuit fabrication.¹⁸⁻¹⁹ Graphene used in inkjet printing can be synthesized via low cost solvent-exfoliation processes to rapidly produce large batches of graphene or graphene oxide flakes that can be subsequently solubilized and formulated into a printable ink.²⁰ Furthermore, the ink jet printing process can be used to make microcircuits with line resolution of approximately 60 μm —thus eliminating the need for UV lithographic techniques that utilize a pre-fabricated photomask with subsequent dry etching of active materials *or* screen printing techniques that use a pre-fabricated metal stencil to pattern surfaces with defined circuit geometries.²¹⁻²² Subsequently inkjet printing has been used for a wide variety of functional devices including thin film transistors,^{19, 23} acoustic actuators,²⁴ dipole antennas,²⁵ and sensors such as a NO_2 , Cl_2 vapor sensor²⁶ and a temperature sensor²⁷. Herein we develop, for the first time, a solid-contact ISE (potassium selective) with IPG. We further demonstrate how the thermal annealing in a nitrogen ambient can increase/enhance the electrical conductivity, porosity, and nitrogen doping of the IPG electrode parameters to improve the potassium sensing capability of the resultant ISE.

Experimental section

Reagents

Valinomycin (90%), Bis(2-ethylhexyl) sebacate (DOS), potassium tetrakis(4-chlorophenyl) borate (KTCIPB), polyvinyl chloride PVC, tetrahydrofuran (THF, 99.8%), sodium chloride (NaCl), sodium sulfate (Na₂SO₄), sodium bicarbonate (NaHCO₃), potassium chloride (KCl), magnesium chloride (MgCl₂), sodium phosphate anhydrous monobasic (NaH₂PO₄), calcium carbonate (CaCO₃) and ammonium hydroxide (NH₄Cl) were procured from Sigma Aldrich (St. Louis, MO). Spiked sweat containing potential interfering electrolytes, including NaCl, Na₂SO₄, NaHCO₃, KCl, MgCl₂, NaH₂PO₄, CaCO₃ and NH₄Cl at physiological concentrations²⁸ were used in the experiments and spiked with potassium concentrations as stated. Artificial eccrine perspiration (stabilized at pH 4.5) was purchased from Pickering Laboratory with a listed concentration of ~ 33 mM. The artificial perspiration contains the following metabolites (uric acid, lactic acid, urea, ammonia), minerals (sodium, iron, nitrate, calcium, copper, sulfate, magnesium, potassium, zinc, chloride) and amino acids (glycine, L-histidine, L-serine, L-alanine, L-isoleucine, L-threonine, L-arginine, L-leucine, L-tyrosine, L-asparagine, L-lysine, L-valine, L-aspartic acid, L-methionine, Taurine, L-citrulline, L-ornithine, L-glutamic, L-phenylalanine) in concentration levels found in real eccrine perspiration.

Graphene ink formulation

Inkjet printable, graphene-based ink was produced from exfoliated graphene powder, solvents, and the stabilizing polymer ethyl cellulose by modifying previously described methods.^{20, 22} Briefly, graphene ink batches (20 mL) were synthesized by vortex mixing single layer dispersible graphene (ACS Materials, “completely” reduced graphene oxidase obtained via the Hummer’s Methods) in a mixture of 85% cyclohexanone (Sigma-aldrich 398241) with 15% Terpineol (Sigma-Aldrich

T3407) for 1 min at high speed in a 25 mL falcon vortex tube. The initial concentration of graphene to solvent was set to 3.5 mg/ml ratio. Ethyl cellulose (Sigma-Aldrich 433837) was subsequently added to the mixture at a ratio of 3.5 mg/mL and the subsequent solution was vortex mixed for 5 minutes. The graphene ink was then poured into a 50-mL beaker and probe sonicated (Sonics Vibra-cell VCX-750 ultrasonic processor) at 50% amplitude 3 times for 30 min, bath sonicated for 6 hours at high power, and finally filtered through a 0.45 μm syringe filter to break up and filter out large graphene particles and ensure a consistently smooth, jettable ink with a measured viscosity of 10 cP with a microVISC RheoSense viscometer.

IPG electrode fabrication

Graphene ink was inkjet printed via a Dimatrix Materials Printer (Model DMP 2800, Fujifilm) while the electrode patterns were designed in AutoCAD (Auto- desk, San Rafael, CA). To print the ink, 3 mL of the formulated graphene ink was loaded into a Diamatrix printer cartridge with 10 pL nominal drop volume nozzles. Printing was conducted on a 6" silicon wafer placed on the printer plate that was maintained at a temperature of 60°C. The printing speed (8 m/s as verified by the dropwatcher) was set by adjusting the nominal drop spacing (40 μm) as well as the nozzle temperature (60°C), waveform, and voltage. The total printed graphene ink layer thickness (i.e., 50 printer passes) on the silicon was measured to be 3.5 μm per a surface profilometer measurement.

Thermal annealing and characterization of printed graphene

The IPG electrodes were subsequently annealed in a nitrogen environment at varying temperatures (200°C, 350°C, 500°C, 650°C, 800°C and 950°C) within a 2" compact split tube furnace (MTI Corp.) for 1 hour. Subsequent Raman spectroscopy, X-ray photoelectron spectroscopy (XPS), field emission scanning electron microscopy (FESEM), and electrical sheet resistance data were

acquired for unannealed and thermally annealed samples. Raman spectroscopy was acquired with a Renishaw spectrometer microscope using a 488-nm excitation source (argon ion laser), a total acquisition time of 30 s (i.e., three acquisition times of 10 s each), and a 200 μ W laser power illumination. The spectrometer was calibrated using an internal silicon reference prior to the measurements. FESEM micrographs were obtained via a FEI Quanta 250 FE-SEM with an electron beam voltage of 10kV. Electrical sheet resistance data were obtained from a signatone four-point probe. The measurements were taken at multiple spots (four different spots) on the sample surface and the average value of these measurements were plotted. The XPS spectra were collected using a Kratos Amicus X-ray Photoelectron Spectrometer using an Al $K\alpha$ excitation source (1486.7 eV). The corresponding photoelectron energies from the constituent elements were measured by subtracting the excitation energy from the scan and subsequently obtaining the binding energy survey scan. The N1s spectrum was analyzed for each distinctly annealed IPG electrodes. A Shirley background fitting and Gaussian Lorentzian line peak fitting on the N1s peak spectrum was performed with a CasaXPS software package.

Potassium ISE synthesis

IPG electrodes were converted into potassium ISEs by depositing a potassium selective membrane onto the graphene. The potassium selective membrane cocktail consisted of 1.0 wt% valinomycin, 66wt% DOS, and 33wt% PVC. The components were dissolved in 1mL THF with concentration of 15wt%. Next, 10 μ L of cocktail was drop coated onto the IPG electrodes and subsequently dried in air for 6 hours.

Potentiometric analysis

The potentiometric measurements were performed using a CHI6273E electrochemical workstation (CHI Instruments, USA). An Ag/AgCl electrode (saturated in 3M KCl) was used as the reference

electrode. The electrodes were conditioned in 0.01M KCl solution for 24 hours before electrochemical testing and dry stored at room temperature between testing experiments. The analytical performance of the potassium ISEs was analyzed in the concentration range of 10^{-8} to 10^{-2} M via a KCl salt solution. The interfering tests were conducted by following similar protocols²⁸ where DI water was first spiked with 0.001M KCl, next with 0.01 M KCl, and finally with artificial eccrine perspiration. IPG ISE drift analysis was performed by constant current chronopotentiometry where the potential was recorded by applying a positive 1 nA current for 100 s followed by a negative current of 1 nA for 100 s in a test vial containing 0.1M KCl solution. The drift of the IPG ISE was derived from the potential change during the recording time ($\Delta E/\Delta t$) when the fixed current applied to the IPG ISE.²⁹

Results and discussion

Potassium IPG ISE fabrication strategy

The potassium ISEs were developed on thermally annealed IPG per the process steps displayed in Figure 1. First, graphene ink was formulated with single layer graphene dispersed in solvent (85% cyclohexanone / 15% terpineol) and stabilized with an ethyl cellulose polymer by both bath and probe sonication as noted in the Experimental Section and by modifying existing graphene ink recipes (Figure 1a).^{20,22} The formulated graphene ink (viscosity of 10 cP) was inkjet printed via a Dimatrix Materials Printer onto a silicon wafer (with 300 nm silicon oxide) (Figure 1b-d & Experimental Section). Next, a split tube furnace was used to anneal the IPG at 200°C, 350°C, 500°C, 650°C, 800°C and 950°C in a nitrogen environment (i.e., without oxygen) to prevent graphene oxidation during the annealing process (Figure 1e). As shown in subsequent electrical and optical characterization experiments this annealing process is conducted to improve the electrical conductivity of the printed graphene and improve its electrochemical sensing

performance. Finally, a potassium ion-selective cocktail (see Experimental section for details) is drop coated onto the circular working electrode comprised of IPG to complete the potassium ISE fabrication protocol.

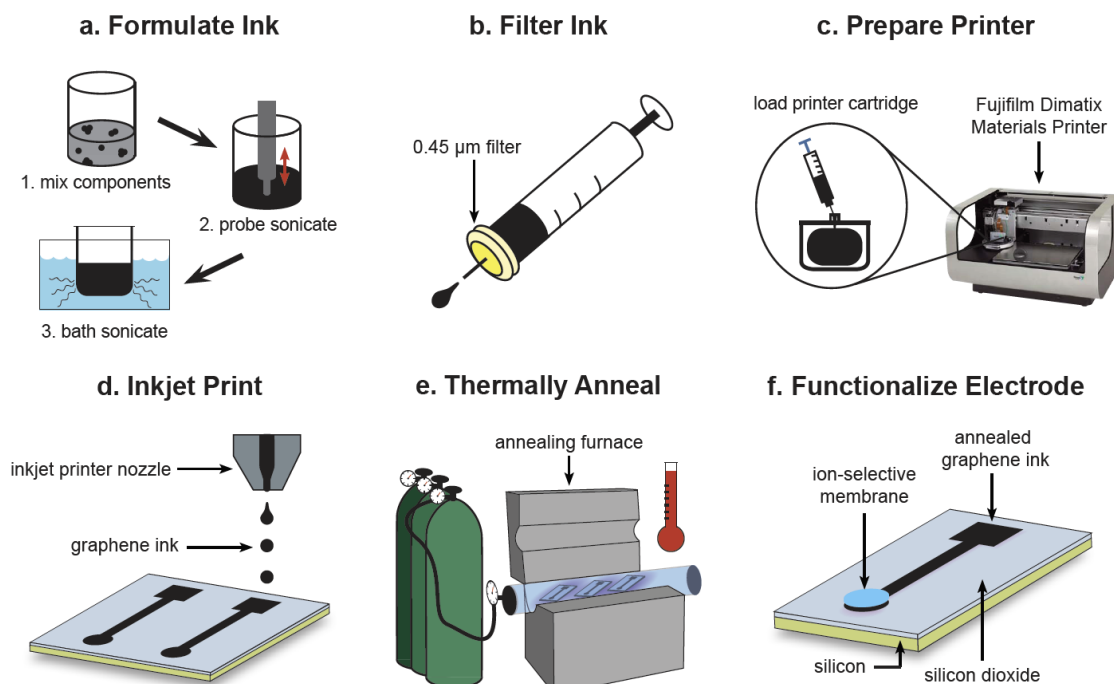


Figure 1. Schematic fabrication diagram of the IPG potassium ISE showing: (a) graphene ink formulation including bath sonication and probe sonication of the graphene powder mixed with the ethyl cellulose binder and solvents cyclohexanone and terpineol; (b) a syringe (0.45 μm mesh size) is used to filter the ink prior to cartridge loading; (c) loading of cartridge with graphene ink onto the inkjet printer; (d) inkjet printing of the graphene electrodes on a Si/SiO₂ (300nm) wafer; (e) thermal annealing of the as-fabricated Si/SiO₂/graphene electrodes in a nitrogen environment; and (f) integration of ion selective membranes on to the circular head of the annealed graphene electrode to form a potassium ISE on the printed graphene.

Characterization of IPG electrodes

Before potassium ISE immobilization, the IPG was thermally annealed and characterized via electrical measurements, Raman spectroscopy, and FESEM (Figure 2). First, the electrical sheet resistances of the IPG electrodes annealed at six distinct temperatures, viz., 200°C, 350°C, 500°C, 650°C, 800°C and 950°C were compared with the sheet resistance of the unannealed graphene electrode (Figure 2a). Figure 2a displays an unannealed IPG sheet resistance of $52.8 \pm$

7.4 M Ω/\square (± 1 stdev.; n=4) that decreases with increasing annealing temperature until a plateau of approximately 147.7 \pm 14.9 Ω/\square (± 1 stdev.; n=3) at 800 $^{\circ}$ C is reached. The sheet resistance slightly increases to 172.7 \pm 33.3 Ω/\square (± 1 stdev.; n=3) when the annealing temperature is raised to 950 $^{\circ}$ C. Thus, there is more than five orders of magnitude increase in the electrical conductivity as the graphene is annealed to a temperature of 800 $^{\circ}$ C. This significant increase in electrical conductivity (equivalently, decrease in the sheet resistance) is most likely due to the further reduction of the reduced graphene oxide flakes, graphitic crystal formation, and nitrogen doping as verified in subsequent FESEM, Raman spectroscopy, and XPS analysis.

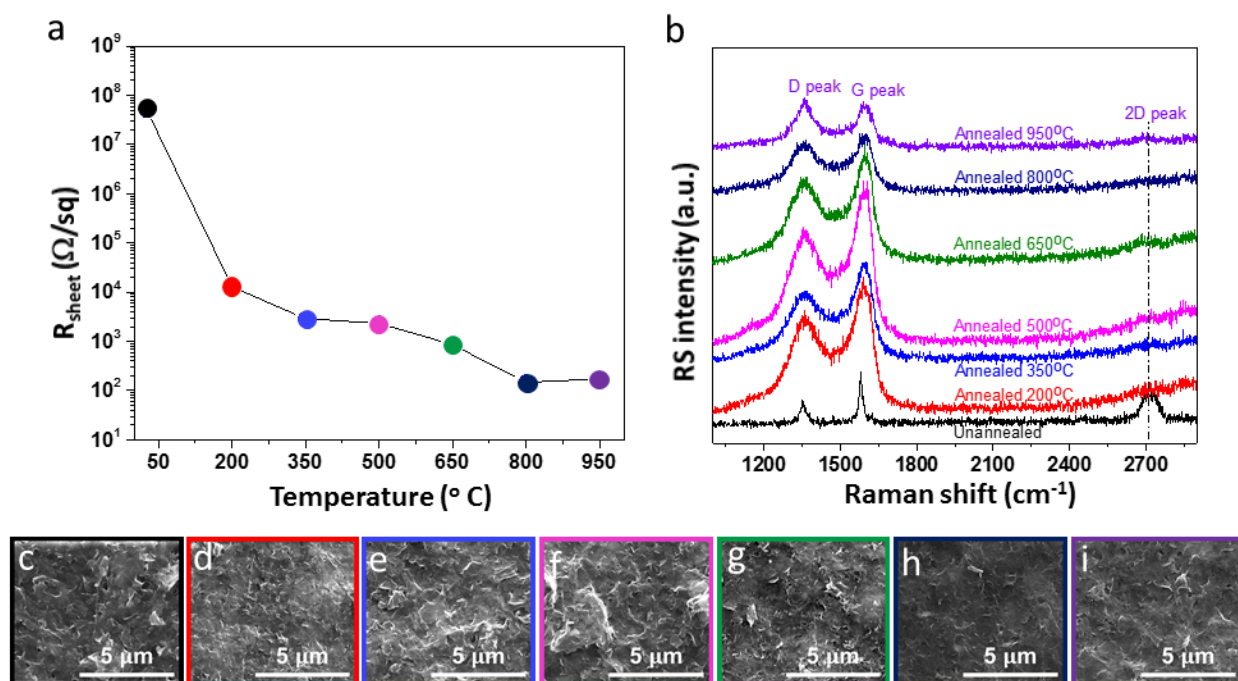


Figure 2. Post-printing thermal annealing in a nitrogen ambient was used to process the graphene IDEs; (a) Electrical sheet resistance vs. annealing temperature of the graphene IDEs. (b) Raman spectra of unannealed and annealed IPG electrodes at distinct temperatures [200 $^{\circ}$ C (red), 350 $^{\circ}$ C (blue), 500 $^{\circ}$ C (pink), 650 $^{\circ}$ C (green), 800 $^{\circ}$ C (dark blue) and 950 $^{\circ}$ C (purple)]. The D, G, as well as 2D peaks are noted in each IPG electrode. FESEM images (lower row, c-i) show the microstructures of the unannealed and thermally annealed printed graphene (color coded boxes around FESEMs correspond to the annealing temperature color legend in Figure 2a and 2b).

Raman spectroscopy was performed on both annealed and unannealed IPG samples (Figure 2b). Raman spectroscopy was employed to analyze the printed graphene as it has been extensively used to characterize both graphene and graphitic materials.³⁰ Single crystal micro-mechanically exfoliated graphene possesses two characteristic peaks, namely a G peak and 2D peak that correspond to wave numbers of approximately 1580 cm^{-1} and 2700 cm^{-1} respectively. Furthermore, edge defect, grain boundary, and/or topological defects in the graphene gives rise to the D peak observed at $\sim 1350\text{ cm}^{-1}$ as often portrayed in jagged petal-like growth of CVD grown multilayered graphene.^{15, 31} In the IPG presented here, the D, G, and 2D peaks are observed at wave numbers of approximately 1350 cm^{-1} , 1590 cm^{-1} and 2700 cm^{-1} respectively. Overall, these three graphene characteristic peaks can be attributed to a defect-rich multilayer graphene stack (the reduced intensity of the 2D peak intensity compared to that of the G peak reveals a multilayer structure, while the D peak intensity reveals a high degree of defects).³² Also, the D and G peaks are red shifted by several tens of wave numbers (the D and G peaks red shifts by $10\text{-}20\text{ cm}^{-1}$) as compared to the typical Raman spectrum for single-layer, single-crystal graphene. This red shift can be attributed to the combination of defects and thermally induced tensile strain in the printed graphene structure as the red shift of the D peak increases with increasing annealing temperature and the red shift of the G and 2D peaks remains stable and temperature independent. Such increasing strain could originate from movement in the defect sites and flake/flake junctions of the printed graphene layers during thermal annealing. In addition to one phonon defect-assisted process, there were also multi-phonon defect-assisted processes such as D+D' peak present in all the electrodes (Figure S1 in the Supplemental Information).³²

The microstructure of the IPG electrodes was also characterized via FESEM (Figure 2c) for both unannealed IPG and IPG annealed at distinct temperatures (200°C , 350°C , 500°C , 650°C ,

800°C and 950°C). The FESEM micrographs reveal the relative roughness of the graphene microstructure of the unannealed IPG. This microstructure does not noticeably change during thermal annealing at 200°C and 350°C (Figure 2d & 2e). However, upon reaching an annealing temperature of 500°C, the graphene microstructure is noticeably more smooth with less exposed graphene flake edges (Figure 2f). At these higher annealing temperatures (500°C), the individual flakes appear to merge together making a smooth microstructure. This ‘thermally induced smoothening’ of the microstructure of the IPG electrode exhibits more than four orders of conductivity enhancement compared to the unannealed electrode as the physical boundaries between individual graphene flakes becomes “welded” together and the defects are minimized. Further increase in the annealing temperature (650°C or greater, Figure 2g – 2i) displays a more porous microstructure in the electrode (see Figure S2 in the Supplemental Section). At these higher annealing temperatures, the D peak of the IPG Raman spectra increases and the sheet resistance further decreases. As the IPG annealing temperature is further increased (800°C or greater) the IPG achieves both a relatively high electrical conductivity and high number of defects that are necessary for fast heterogeneous charge transport which can subsequently lead to highly sensitive electrochemical sensing/biosensing. The presence of more defects at higher temperatures, relating to the porous micro/nano structure, is further evidenced from the Raman spectra at higher temperature (increasing trend of the ratio of D peak intensity to G peak intensity).

To further probe the local electronic structure, the N 1s photoelectron spectra of all the annealed electrodes under consideration were analyzed via XPS (Figure 3). Note that an unannealed sample does not have a nitrogen peak as shown previously.³³ However, all the annealed electrodes, including the IPG annealed at 200°C, contain nitrogen (Figure 3). Figure 3d shows the total nitrogen atomic percentage doped in graphene with minimum of 0.4 at. % at 200 °C and

maximum of 1.1 at. % at 350 °C. Such N 1s peaks at 400 eV (blue lines/points in Figure 3) are consistent with nitrogen bonded with graphene lattice defects (nitrogen atom substitutional doped in graphene lattice)³⁴⁻³⁵. It is interesting to note that the formation of nitrogen doping within the graphene lattice (alternatively called ‘quaternary nitrogen’) has been realized before in reduced graphene oxide matrices using ammonia annealing at a temperature of 900°C, however in this work the IPG electrodes exhibits nitrogen doped graphene (NG) at much lower temperatures (200°C) in a nitrogen annealed ambient. A higher binding energy N 1s component can also be found at 402 eV (red lines/points in Figure 3) in the thermally annealed IPG which is consistent with nitrogen that contains a higher coordination number. Such higher binding energy N 1s components are presumably formed via substitution with the carbon atoms in the graphene lattice (this type of coordination has been reported to be an ‘oxidized nitrogen’ phase^{34, 36}). The higher binding energy component gains more intensity as annealing temperature increases, however, the relative nitrogen doping in graphene displays a decreasing graphitic coordination with increasing temperature (Figure 3c). Finally, to collectively understand the role of nitrogen annealing at various temperatures from a defect generation standpoint the (I_D/I_G) intensity ratio from the Raman spectroscopy data originally displayed in Figure 2b was plotted versus total atomic nitrogen concentration (see Figure 3d). The IPG defects, as denoted in the I_D/I_G ratio plot (greater I_D/I_G signifies more defects and vice versa), continue to rise with an increasing rate according to annealing temperature while the total nitrogen doping increases to a maximum (350°C) and then decreases with higher annealing temperatures. Thus, the concomitance of increasing superficial defects and a lower level of overall nitrogen composition, i.e., a more graphitic surface, may have led to higher electrical conductivity in high temperature annealed IPG (800°C or higher) as well as to the higher electrochemical potassium sensing capability (see subsequent sections).

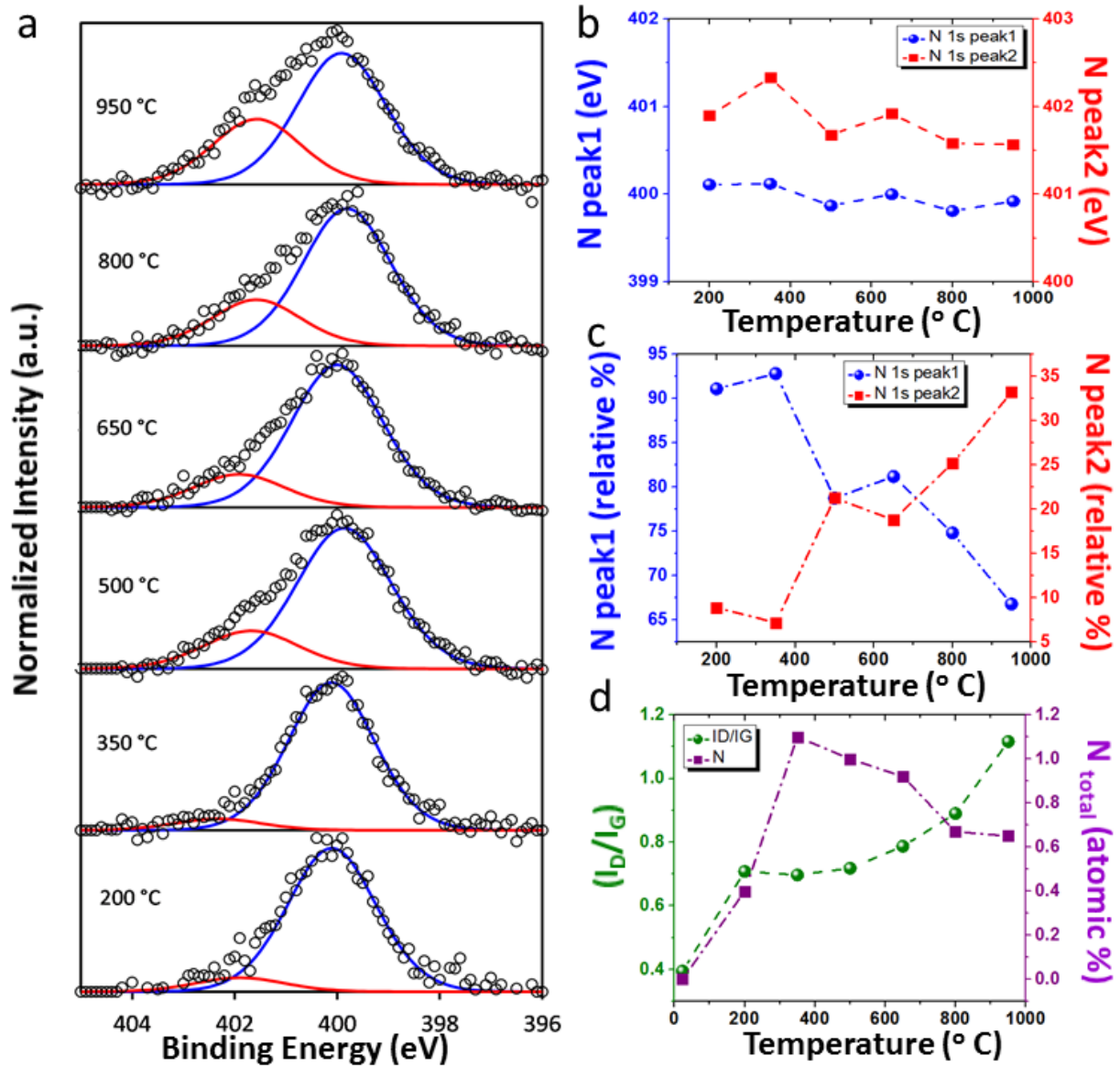


Figure 3. (a) X-ray photoelectron spectroscopy of IPG annealed at various temperatures show emergence of two peaks, a N 1s peak at 400 eV (blue line, peak 1) and a higher order N1 s peak at 402 eV (red line, peak 2); (b) the position of the N 1s peak 1 and peak 2 with respect to annealing temperature; (c) the relative atomic percentage of nitrogen doping on the IPG with respect to annealing temperature and (d) variation of Raman intensity ratio (I_D/I_G) and total nitrogen doping (atomic percentage) with respect to temperature.

Electrochemical analysis of potassium ISE

The IPG was converted into a potassium ion selective electrode by drop coating a potassium selective membrane cocktail (containing valinomycin as the potassium ionophore) onto the graphene electrodes that were thermally annealed at 200°C, 350°C, 500°C, 650°C, 800°C and 950°C (see Experimental Section, also note the unannealed IPG electrodes were not sufficiently conductive for electrochemical sensing and hence were not tested in these experiments). The electrochemical ionic response to potassium of the IPG ISE was measured in DI water with various concentrations of KCl solutions vs. an Ag/AgCl reference electrode (Experimental Section). Experimental results show that with increasing annealing temperature, the IPG ISE sensors achieve lower detection limits (Figure 4a) and increased sensitivity (Figure 4b). More specifically, the detection limit of the IPG ISE sensor steadily decreases from 22 μM ($\text{Log}_{10}\text{K}^+=10^{-4.6}$) to 7 μM ($\text{Log}_{10}\text{K}^+=10^{-5.2}$) as the annealing temperature increases to 950°C. The sensitivity values of IPG ISEs also increase and display less variability from 48.6 mV to 57.6 mV with increasing annealing temperature. Thus, when the annealing temperature of IPG electrodes reaches 800°C, the ISE sensors begin to exhibit a sensitivity value close to that predicted by the Nernstian equation. Furthermore the overall sensor drift (Figure 4c), as measured via chronopotentiometry³⁷, continued to decrease to 8.6×10^{-6} V/s as the annealing temperature increased to 800°C.

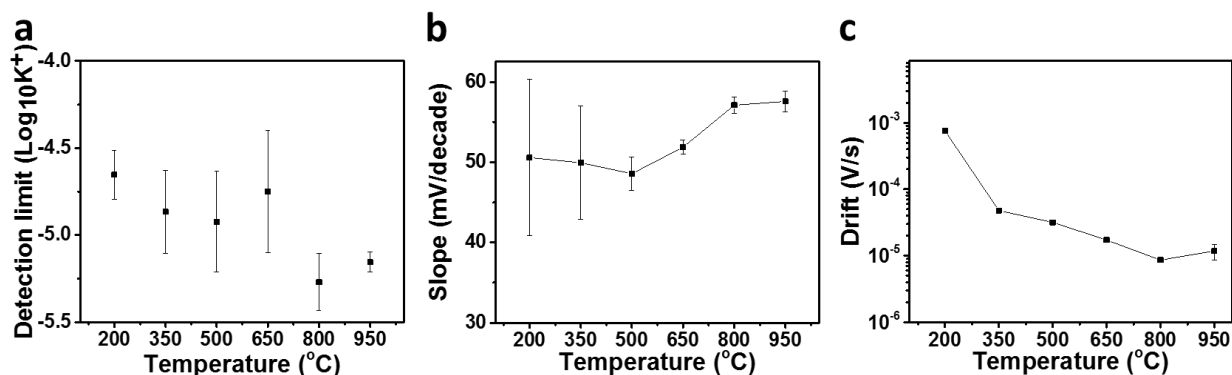


Figure 4. Potassium ion sensing with the IPG ISEs annealed at distinct temperatures (200°C, 350°C, 500°C, 650°C, 800°C, and 950°C). Graphs depicting the average sensor characteristics i.e., (a) detection limit, (b) sensitivity (slope of sensing range) and (c) the drift with standard error (n=3).

The decreases in the IPG ISE detection limit and drift with higher annealing temperature could be explained in part by the smoother thermal annealed IPG surface minimizing the spontaneous formation of a water layer between the ISE membrane and IPG electrode. Such a water layer acts as an electrolyte reservoir which re-equilibrates on each sample composition change, consequently introducing potential instability and higher detection limits³⁸. At annealing temperatures of 200°C and 350°C, the rough IPG microstructured surface is more conducive to water layer formation within the more rugged graphene flake topology. This water layer formation could explain the higher variation of sensitivity value for IPG ISEs annealed at the lower temperatures of 200°C and 350°C. However, as the annealing temperature increases, the microstructure of the graphene flakes becomes much more smooth which in turn could reduce the formation of water layer build-up and hence lower the drift and detection limit of the ISE.

Based on the electrochemical characterization, the ISE based on IPG thermally annealed at 950°C were chosen for further characterization. This graphene potassium ISE exhibited a Nernstian response to KCl corresponding to a sensitivity value of 57.6 mV per decade of K⁺

concentration, a characteristic that is predicted by the theory for solvent polymeric membranes doped with valinomycin as the potassium ionophore.³⁹ As shown in Figure 4a, the ISE displayed a linear response to K^+ concentration (in logarithmic scale) within the KCl concentration range of 0.01mM to 10 mM. The small standard deviation even between the lowest concentrations of potassium (i.e., R.S.D.: 2.27%, n=3: see Figure 4a) yielded a reliable and repeatable observable detection limit of 7 μ M ($\text{Log}_{10} K^+ = -5.2$). The potential versus $\text{log}_{10} K^+$ plot reveals that the sensing response is nearly instantaneous and reaches the stability within 10s, a response time faster than that of a liquid-contact ion-selective electrode, especially at lower concentrations.⁴⁰ (Figure 5a inset). Such a fast response is important for the real time monitoring of rapid changes in potassium concentration in the sweat that can fluctuate quickly according to perspiration rates.⁴¹ Furthermore, the IPG ISE was also tested for repeatability by subjecting the sensor to successive changes in KCl solutions with potassium concentrations alternating from 1 mM, 10 mM, and 100 mM, using four oscillation cycles (see Figure S3 in Supporting Information). This improvement in potassium sensitivity and detection limit is most likely due to reduced water layer formation as previously described, but also do to the increasing porosity of the graphene with higher annealing temperatures (see Figure S2 in the Supporting Information). Such higher porosity or edge defects in graphene render the surface more electroactive than pristine basal plane graphene,¹⁵ and subsequently most likely led to improvements in the capacitance and charge storage capability of the electrodes and the near Nernstian slope/sensitivity.⁵⁷⁻⁵⁸

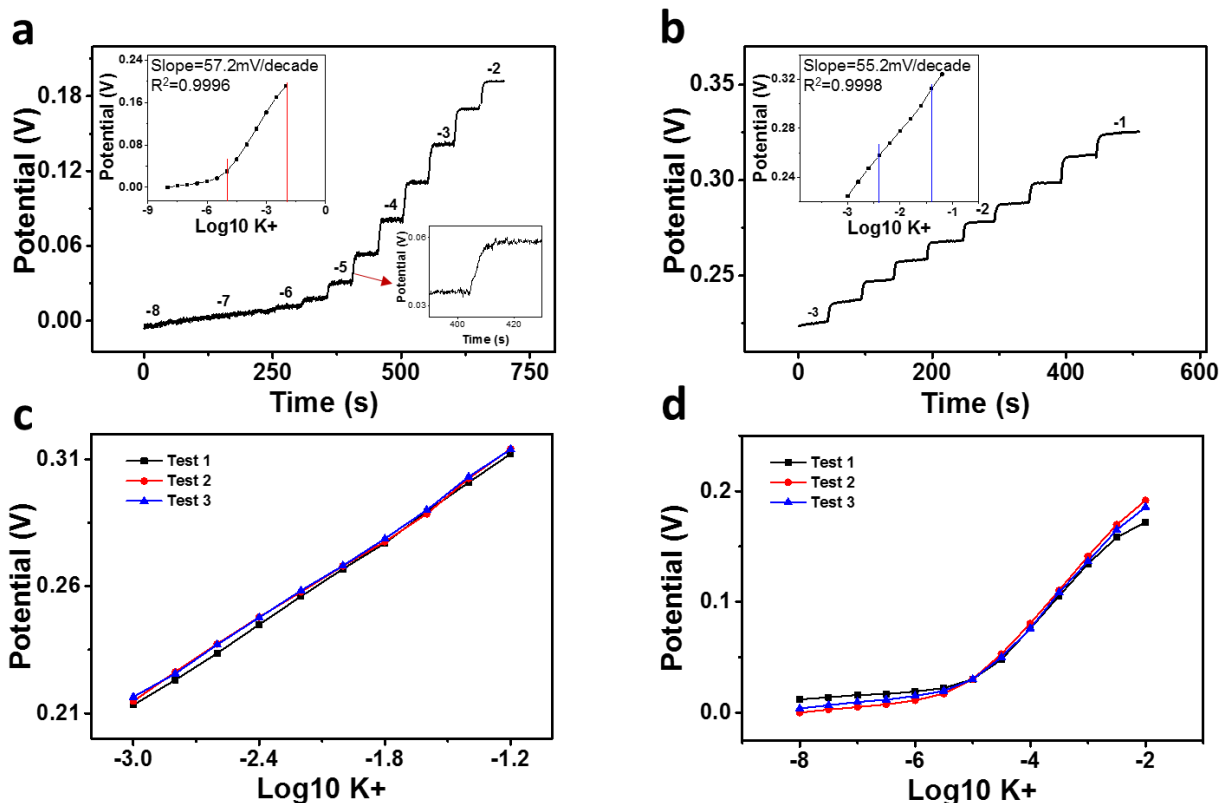


Figure 5. (a) Potassium calibration plot for the IPG electrodes annealed at a temperature of 950°C portraying potential response changes for successive increases in potassium concentration (10^{-8} M, $10^{-7.5}$ M, 10^{-7} M, $10^{-6.5}$ M, 10^{-6} M, $10^{-5.5}$ M, 10^{-5} M, $10^{-4.5}$ M, 10^{-4} M, $10^{-3.5}$ M, 10^{-3} M, $10^{-2.5}$ M, and 10^{-2} M) in DI water (b) and successive increases in potassium concentration (10^{-3} M, $10^{-2.8}$ M, $10^{-2.6}$ M, $10^{-2.4}$ M, $10^{-2.2}$ M, 10^{-2} M, $10^{-1.8}$ M, $10^{-1.6}$ M, $10^{-1.4}$ M, $10^{-1.2}$ M) in sweat. Corresponding potential vs. concentration profiles for potassium concentration sensing in (c) DI water and (d) in artificial perspiration showing sensor reproducibility for three distinct potassium calibration plots performed with the same graphene ISE.

The developed potassium ISE was also tested against the backdrop of common ion interferences that are typically found in sweat²⁸. These initial selectivity experiments were conducted in by spiking DI water with said interferences (at concentration levels typically found in sweat) while the potassium concentration was varied over the sweat potassium physiological range of 1 mM to 63 mM (Figure 5b)⁴¹. The potassium ISE sensor showed a Nernstian response with the sensitivity value of 54.5 mV per decade of potassium ion concentration (R.S.D.: 0.91%, n=3). The obtained potassium sensitivity obtained was also similar to the sensitivity of K^+ ions

previously demonstrated in the KCl solution. The small standard deviation of sensitivity value between experiments conducted in KCl solution (R.S.D.: 2.27%, n=3: see Figure 5c) and KCl solution with multiple additive ions (R.S.D.: 0.91%, n=3: see Figure 5d) showed both experiments contained a high-level of repeatability. The selectivity of the ISE is mainly determined by the composition of the membrane and not directly influenced by the type of solid contact used.⁴² The selectivity coefficients, $\log K_{KJ}^{pot} \pm$ standard deviation ($n=3$), of common interfering ions [i.e., sodium (Na), magnesium (Mg), and calcium (Ca)] were also obtained, according to previously reported protocols^{42,39} as follows: $\log K_{KNa}^{pot} = 3.57 \pm 0.12$, $\log K_{KMg}^{pot} = 3.90 \pm 0.08$, $\log K_{KCa}^{pot} = 3.39 \pm 0.21$. The obtained selectivity coefficient is comparable to other carbon based solid contact ISE.⁴³⁻⁴⁶ Furthermore, the IPG ISE was capable of accurately detecting the amount of potassium found within artificial eccrine perspiration (Figure S3 in Supplemental Information) where the measured potentiometric response correlated to a potassium concentration of 33.9 ± 2.4 mM—a potassium concentration that is close to the listed value of 33 mM (see Figure S4 in Supplemental Information & the Experimental Section). This result demonstrates that the IPG ISE is capable of selectively detecting potassium within a complex matrix containing a combination of 33 metabolites, minerals, and amino acids (see Experimental Section).

Finally, the potassium sensing results of the IPG ISE was compared with similar carbon-based electrodes that have been recently published in the research literature (Table 1). For example, the potassium detection limit of the IPG ISE reached $\text{Log}_{10}K^+=10^{-5.2}$, which is lower than similar ISEs comprised with nanostructured with carbon fullerene ($\text{Log}_{10}K^+=10^{-5.0}$) and graphene on glassy carbon ($\text{Log}_{10}K^+=10^{-4.5}$)⁴⁴. The recorded drift (8.6×10^{-6} V/s) of the IPG ISE is lower than similar ISEs nanostructured with CNTs (1.7×10^{-5} V/s) and graphene on glassy carbon (1.2×10^{-5} V/s)⁴⁴⁻⁴⁵. The linear sensing range (0.01 mM to 10 mM) of the developed IPG ISE is also on

par with similar solid-state potassium ISE that use nanocarbon-based materials as the transduction element⁴³⁻⁴⁷.

Table 1. Performance comparison table of nanocarbon-based, solid-state ISEs

Electrode	Detection Limit (M)	Slope (mV/decade)	Linear Range (M)	Drift (V/s)	Ref
IPG	$10^{-5.2}$	57.2	$10^{-5} \sim 10^{-2}$	$*8.6 \times 10^{-6}$	This work
Fullerene	$10^{-5.0}$	55	$10^{-5} \sim 10^{-2}$	-	46
CNT	$10^{-5.5}$	58.4	$10^{-5.5} \sim 10^{-2.5}$	$*1.7 \times 10^{-5}$	45
Graphene/GC	10^{-5}	59.2	$10^{-4.5} \sim 10^{-1}$	$*1.2 \times 10^{-5}$	44
CIM carbon	$10^{-5.6}$	59.5	$10^{-5.2} \sim 10^{-1}$	$^{\Psi}4.7 \times 10^{-3}$	47
Porous carbon	$10^{-5.7}$	57.8	$10^{-5} \sim 10^{-1}$	$^{\zeta}14.9 \times 10^{-3}$	43, 48

*This reported drift was obtained via chronopotentiometric means (see Experimental Section).

^Ψ Long range drift test acquired by monitoring the open circuit potential over a timeframe of 70hrs.

^ζ Long range drift test acquired by monitoring the open circuit potential over a timeframe of 20hrs.

IPG: Inkjet Printed Graphene

CNT: Carbon Nanotube

GC: Glassy Carbon

CIM carbon: Colloid-Imprinted Mesoporous Carbon

Conclusions

In summary, we have developed a scalable inkjet printing process for graphene-based ion selective electrodes or IPG ISEs. Before functionalization with a potassium detecting ionophore, the IPG was thermally annealed in a nitrogen environment to improve both the electrical conductivity and electrochemical sensing capability of the resultant IPG ISE. This annealing process improved the electrical sheet resistance of the IPG by several orders of magnitude from $52.8 \pm 7.4 \text{ M}\Omega/\square$ for unannealed IPG to $147.7 \pm 14.9 \text{ }\Omega/\square$ $172.7 \pm 33.3 \text{ }\Omega/\square$ for IPG annealed at temperatures of 800°C and 950°C respectively. Furthermore, the thermal annealing process created a highly conductive graphene surface that is well-suited for electrochemical sensing as the

“welded porous” surface is sufficiently “electroactive” without the need for graphene chemical modification steps such as metallic nanoparticle integration which is often used to increase the electroactive nature of carbon-based electrochemical electrodes.⁴⁹⁻⁵³ The IPG electrodes were subsequently converted into potassium ISEs by functionalizing the graphene surface with the potassium ionophore, valinomycin, drop coated within a PVC matrix. The resultant IPG ISE, thermally annealed at 950°C, displayed a wide linear sensing range (0.01mM to 10 mM) and low detection limit (7 μ M) that fared favorably to other potassium ISEs that used a nanocarbon-based transduction element (e.g., graphene on glassy carbon electrodes, carbon nanotubes and mesoporous carbon; see Table 1). Furthermore, the inkjet printing process developed herein presents a scalable nonmanufacturing route for nanostructured ISEs that eliminates the need for both the costly fabrication of graphene through chemical or physical vapor deposition, the need for costly electrode patterning through clean room process such as photolithography, and the need to fabricate metal stencils for each new pattern design such as performed in screen printing. The developed potassium IPG ISE was capable of measuring potassium in a complex artificial eccrine perspiration solution that contained a combination of 33 metabolites, minerals, and amino acids and displays a potassium linear sensing range. The IPG ISE is also capable of sensing physiologically relevant concentrations of potassium including those found in plasma and serum where potassium concentrations can range between 3.1 and 4.6 mM and 0.3–0.4 mM respectively⁵⁴. Also, the developed IPG ISE could potentially be used to detect plant available potassium levels in soil (1.1-2.2% of the 10 – 20 g of potassium found in a typical kg of soil is plant available⁵⁵) where a typical soil slurry dilution (1kg of soil per 2 L of water) would yield a potassium concentration range from 1.4 mM to 5.7 mM. Due to the potential to print graphene on flexible, curvilinear surfaces³² as well as the ability to detect concentrations of potassium found in

sweat [$\sim 1\text{mM}^{56}$], the developed potassium ISEs may also be well-suited for wearable epidermal sensors that monitor potassium levels from eccrine sweat glands. Of course, in all of these potassium sensing examples, rigorous testing within field conditions will need to be conducted to prove the viability of the IPG ISE in these various environments where temperature, humidity, and interfering species may vary widely. Such rigorous testing is reserved for future work. In summary, the developed potassium IPG ISEs represent a potential scalable, low-cost manufacturing protocol for monitoring potassium in a variety of biomedical and environmental applications.

References

1. Pumera, M.; Ambrosi, A.; Bonanni, A.; Chng, E. L. K.; Poh, H. L., Graphene for Electrochemical Sensing and Biosensing. *TrAC, Trends Anal. Chem.* **2010**, *29* (9), 954-965.
2. Song, Y.; Luo, Y.; Zhu, C.; Li, H.; Du, D.; Lin, Y., Recent Advances in Electrochemical Biosensors Based on Graphene Two-Dimensional Nanomaterials. *Biosens. Bioelectron.* **2016**, *76*, 195-212.
3. Fang, Y.; Wang, E., Electrochemical Biosensors on Platforms of Graphene. *Chem. Commun.* **2013**, *49* (83), 9526-9539.
4. Geim, A. K.; Novoselov, K. S., The Rise of Graphene. *Nat Mater* **2007**, *6* (3), 183-191.
5. Ping, J.; Zhou, Y.; Wu, Y.; Papper, V.; Boujday, S.; Marks, R. S.; Steele, T. W. J., Recent Advances in Aptasensors Based on Graphene and Graphene-Like Nanomaterials. *Biosens. Bioelectron.* **2015**, *64*, 373-385.
6. Soldano, C.; Mahmood, A.; Dujardin, E., Production, Properties and Potential of Graphene. *Carbon* **2010**, *48* (8), 2127-2150.
7. Zhu, Y.; Murali, S.; Cai, W.; Li, X.; Suk, J. W.; Potts, J. R.; Ruoff, R. S., Graphene and Graphene Oxide: Synthesis, Properties, and Applications. *Adv. Mater.* **2010**, *22* (35), 3906-3924.
8. Chou, A.; Böcking, T.; Singh, N. K.; Gooding, J. J., Demonstration of the Importance of Oxygenated Species at the Ends of Carbon Nanotubes for Their Favourable Electrochemical Properties. *Chem. Commun.* **2005**, (7), 842-844.
9. Davies, T. J.; Moore, R. R.; Banks, C. E.; Compton, R. G., The Cyclic Voltammetric Response of Electrochemically Heterogeneous Surfaces. *J. Electroanal. Chem.* **2004**, *574* (1), 123-152.
10. Park, S.; Ruoff, R. S., Chemical Methods for the Production of Graphenes. *Nat. Nanotechnol.* **2009**, *4* (4), 217-224.
11. Premkumar, J.; Khoo, S. B., Electrocatalytic Oxidations of Biological Molecules (Ascorbic Acid and Uric Acids) at Highly Oxidized Electrodes. *J. Electroanal. Chem.* **2005**, *576* (1), 105-112.
12. Tang, L.; Wang, Y.; Li, Y.; Feng, H.; Lu, J.; Li, J., Preparation, Structure, and Electrochemical Properties of Reduced Graphene Sheet Films. *Adv. Funct. Mater.* **2009**, *19* (17), 2782-2789.

13. Sheng, Z.-H.; Zheng, X.-Q.; Xu, J.-Y.; Bao, W.-J.; Wang, F.-B.; Xia, X.-H., Electrochemical Sensor Based on Nitrogen Doped Graphene: Simultaneous Determination of Ascorbic Acid, Dopamine and Uric Acid. *Biosens. Bioelectron.* **2012**, *34* (1), 125-131.
14. Wang, Y.; Shao, Y.; Matson, D. W.; Li, J.; Lin, Y., Nitrogen-Doped Graphene and Its Application in Electrochemical Biosensing. *ACS Nano* **2010**, *4* (4), 1790-1798.
15. Claussen, J. C.; Kumar, A.; Jaroch, D. B.; Khawaja, M. H.; Hibbard, A. B.; Porterfield, D. M.; Fisher, T. S., Nanostructuring Platinum Nanoparticles on Multilayered Graphene Petal Nanosheets for Electrochemical Biosensing. *Advanced Functional Materials* **2012**, *22* (16), 3399-3405.
16. Xu, C.; Wang, X.; Zhu, J., Graphene–Metal Particle Nanocomposites. *J. Phys. Chem. C* **2008**, *112* (50), 19841-19845.
17. Novoselov, K. S.; Fal, V.; Colombo, L.; Gellert, P.; Schwab, M.; Kim, K., A Roadmap for Graphene. *Nature* **2012**, *490* (7419), 192-200.
18. Gao, Y.; Shi, W.; Wang, W.; Leng, Y.; Zhao, Y., Inkjet Printing Patterns of Highly Conductive Pristine Graphene on Flexible Substrates. *Industrial & Engineering Chemistry Research* **2014**, *53* (43), 16777-16784.
19. Torrisi, F.; Hasan, T.; Wu, W.; Sun, Z.; Lombardo, A.; Kulmala, T. S.; Hsieh, G.-W.; Jung, S.; Bonaccorso, F.; Paul, P. J.; Chu, D.; Ferrari, A. C., Inkjet-Printed Graphene Electronics. *ACS Nano* **2012**, *6* (4), 2992-3006.
20. Li, J.; Ye, F.; Vaziri, S.; Muhammed, M.; Lemme, M. C.; Östling, M., Efficient Inkjet Printing of Graphene. *Adv. Mater.* **2013**, *25* (29), 3985-3992.
21. Ping, J.; Wu, J.; Wang, Y.; Ying, Y., Simultaneous Determination of Ascorbic Acid, Dopamine and Uric Acid Using High-Performance Screen-Printed Graphene Electrode. *Biosens. Bioelectron.* **2012**, *34* (1), 70-76.
22. Secor, E. B.; Prabhumirashi, P. L.; Puntambekar, K.; Geier, M. L.; Hersam, M. C., Inkjet Printing of High Conductivity, Flexible Graphene Patterns. *J. Phys. Chem. Lett.* **2013**, *4* (8), 1347-1351.
23. Lim, S.; Kang, B.; Kwak, D.; Lee, W. H.; Lim, J. A.; Cho, K., Inkjet-Printed Reduced Graphene Oxide/Poly(Vinyl Alcohol) Composite Electrodes for Flexible Transparent Organic Field-Effect Transistors. *J. Phys. Chem. C* **2012**, *116* (13), 7520-7525.
24. Shin, K.-Y.; Hong, J.-Y.; Jang, J., Flexible and Transparent Graphene Films as Acoustic Actuator Electrodes Using Inkjet Printing. *Chem. Commun.* **2011**, *47* (30), 8527-8529.
25. Shin, K.-Y.; Hong, J.-Y.; Jang, J., Micropatterning of Graphene Sheets by Inkjet Printing and Its Wideband Dipole-Antenna Application. *Adv. Mater.* **2011**, *23* (18), 2113-2118.
26. Dua, V.; Surwade, S. P.; Ammu, S.; Agnihotra, S. R.; Jain, S.; Roberts, K. E.; Park, S.; Ruoff, R. S.; Manohar, S. K., All-Organic Vapor Sensor Using Inkjet-Printed Reduced Graphene Oxide. *Angew. Chem. Int. Ed.* **2010**, *49* (12), 2154-2157.
27. Kong, D.; Le, L. T.; Li, Y.; Zunino, J. L.; Lee, W., Temperature-Dependent Electrical Properties of Graphene Inkjet-Printed on Flexible Materials. *Langmuir* **2012**, *28* (37), 13467-13472.
28. Harvey, C. J.; LeBouf, R. F.; Stefaniak, A. B., Formulation and Stability of a Novel Artificial Human Sweat under Conditions of Storage and Use. *Toxicol. in Vitro* **2010**, *24* (6), 1790-1796.
29. Ping, J.; Wang, Y.; Wu, J.; Ying, Y., Development of an All-Solid-State Potassium Ion-Selective Electrode Using Graphene as the Solid-Contact Transducer. *Electrochem. Commun.* **2011**, *13* (12), 1529-1532.
30. Ferrari, A. C.; Meyer, J. C.; Scardaci, V.; Casiraghi, C.; Lazzeri, M.; Mauri, F.; Piscanec, S.; Jiang, D.; Novoselov, K. S.; Roth, S.; Geim, A. K., Raman Spectrum of Graphene and Graphene Layers. *Phys. Rev. Lett.* **2006**, *97* (18), 187401.
31. Shang, N. G.; Papakonstantinou, P.; McMullan, M.; Chu, M.; Stamboulis, A.; Potenza, A.; Dhesi, S. S.; Marchetto, H., Catalyst-Free Efficient Growth, Orientation and Biosensing Properties of Multilayer Graphene Nanoflake Films with Sharp Edge Planes. *Adv. Funct. Mater.* **2008**, *18* (21), 3506-3514.
32. Ferrari, A. C.; Basko, D. M., Raman Spectroscopy as a Versatile Tool for Studying the Properties of Graphene. *Nat Nano* **2013**, *8* (4), 235-246.

33. Das, S. R.; Nian, Q.; Cargill, A. A.; Hondred, J. A.; Ding, S.; Saei, M.; Cheng, G. J.; Claussen, J. C., 3D Nanostructured Inkjet Printed Graphene via UV-Pulsed Laser Irradiation Enables Paper-Based Electronics and Electrochemical Devices. *Nanoscale* **2016**, *8* (35), 15870-15879.
34. Sheng, Z.-H.; Shao, L.; Chen, J.-J.; Bao, W.-J.; Wang, F.-B.; Xia, X.-H., Catalyst-free synthesis of nitrogen-doped graphene via thermal annealing graphite oxide with melamine and its excellent electrocatalysis. *ACS nano* **2011**, *5* (6), 4350-4358.
35. Li, X.; Wang, H.; Robinson, J. T.; Sanchez, H.; Diankov, G.; Dai, H., Simultaneous Nitrogen Doping and Reduction of Graphene Oxide. *J. Am. Chem. Soc.* **2009**, *131* (43), 15939-15944.
36. Xu, F.; Minniti, M.; Barone, P.; Sindona, A.; Bonanno, A.; Oliva, A., Nitrogen Doping of Single Walled Carbon Nanotubes by Low Energy Ion Implantation. *Carbon* **2008**, *46* (11), 1489-1496.
37. Bobacka, J., Potential Stability of All-Solid-State Ion-Selective Electrodes Using Conducting Polymers as Ion-To-Electron Transducers. *Anal. Chem.* **1999**, *71* (21), 4932-4937.
38. Bakker, E.; Pretsch, E., Potentiometric Sensors for Trace-Level Analysis. *TrAC, Trends Anal. Chem.* **2005**, *24* (3), 199-207.
39. Bakker, E.; Pretsch, E.; Bühlmann, P., Selectivity of Potentiometric Ion Sensors. *Anal. Chem.* **2000**, *72* (6), 1127-1133.
40. Sutter, J.; Radu, A.; Peper, S.; Bakker, E.; Pretsch, E., Solid-Contact Polymeric Membrane Electrodes with Detection Limits in the Subnanomolar Range. *Anal. Chim. Acta* **2004**, *523* (1), 53-59.
41. Sonner, Z.; Wilder, E.; Heikenfeld, J.; Kasting, G.; Beyette, F.; Swaile, D.; Sherman, F.; Joyce, J.; Hagen, J.; Kelley-Loughnane, N.; Naik, R., The Microfluidics of the Eccrine Sweat Gland, Including Biomarker Partitioning, Transport, and Biosensing Implications. *Biomicrofluidics* **2015**, *9* (3), 031301.
42. Mousavi, Z.; Bobacka, J.; Lewenstam, A.; Ivaska, A., Poly (3, 4-ethylenedioxythiophene)(PEDOT) Doped with Carbon Nanotubes as Ion-To-Electron Transducer in Polymer Membrane-Based Potassium Ion-Selective Electrodes. *J. Electroanal. Chem.* **2009**, *633* (1), 246-252.
43. Ye, J.; Li, F.; Gan, S.; Jiang, Y.; An, Q.; Zhang, Q.; Niu, L., Using sp²-C Dominant Porous Carbon Sub-Micrometer Spheres as Solid Transducers in Ion-Selective Electrodes. *Electrochem. Commun.* **2015**, *50*, 60-63.
44. Li, F.; Ye, J.; Zhou, M.; Gan, S.; Zhang, Q.; Han, D.; Niu, L., All-Solid-State Potassium-Selective Electrode Using Graphene as the Solid Contact. *Analyst* **2012**, *137* (3), 618-623.
45. Crespo, G. A.; Macho, S.; Rius, F. X., Ion-Selective Electrodes Using Carbon Nanotubes as Ion-To-Electron Transducers. *Anal. Chem.* **2008**, *80* (4), 1316-1322.
46. Fouskaki, M.; Chaniotakis, N., Fullerene-Based Electrochemical Buffer Layer for Ion-Selective Electrodes. *Analyst* **2008**, *133* (8), 1072-1075.
47. Hu, J.; Zou, X. U.; Stein, A.; Bühlmann, P., Ion-Selective Electrodes with Colloid-Imprinted Mesoporous Carbon as Solid Contact. *Anal. Chem.* **2014**, *86* (14), 7111-7118.
48. Paczosa-Bator, B., All-Solid-State Selective Electrodes Using Carbon Black. *Talanta* **2012**, *93*, 424-427.
49. Claussen, J. C.; Kumar, A.; Jaroch, D. B.; Khawaja, M. H.; Hibbard, A. B.; Porterfield, D. M.; Fisher, T. S., Nanostructuring Platinum Nanoparticles on Multilayered Graphene Petal Nanosheets for Electrochemical Biosensing. *Adv. Funct. Mater.* **2012**, *22* (16), 3399-3405.
50. Marr, K. M.; Chen, B.; Mootz, E. J.; Geder, J.; Pruessner, M.; Melde, B. J.; Vanfleet, R. R.; Medintz, I. L.; Iverson, B. D.; Claussen, J. C., High Aspect Ratio Carbon Nanotube Membranes Decorated with Pt Nanoparticle Urchins for Micro Underwater Vehicle Propulsion via H₂O₂ Decomposition. *ACS nano* **2015**, *9* (8), 7791-7803.
51. Daniele, M. A.; Pedrero, M.; Burrs, S.; Chaturvedi, P.; Salim, W. W. A. W.; Kuralay, F.; Campuzano, S.; McLamore, E.; Cargill, A. A.; Ding, S., Hybrid Metallic Nanoparticles: Enhanced Bioanalysis and Biosensing via Carbon Nanotubes, Graphene, and Organic Conjugation. In *Nanobiosensors and Nanobioanalyses*, 1st ed.; Springer: Japan, **2015**, pp 137-166.
52. Taguchi, M.; Schwab, N.; Rong, Y.; Vanegas, D.; Garland, N.; Tan, M.; Yamaguchi, H.; Claussen, J.; McLamore, E., PulsED: Pulsed Sono-electrodeposition of Fractal Nanoplatinum for Enhancing Amperometric Biosensor Performance. *Analyst* **2016**, *141* (11), 3367-3378.

53. Claussen, J. C.; Hengenius, J. B.; Wickner, M. M.; Fisher, T. S.; Umulis, D. M.; Porterfield, D. M., Effects of Carbon Nanotube-tethered Nanosphere Density on Amperometric Biosensing: Simulation and Experiment. *J. Phys. Chem. C* **2011**, *115* (43), 20896-20904.
54. Penney, M., Sodium, Water and Potassium. In *Clinical biochemistry, metabolic and clinical aspects.*, 1st ed.; Churchill Livingstone: Edinburgh, **1995**, pp 25-60.
55. Zörb, C.; Senbayram, M.; Peiter, E., Potassium in Agriculture–Status and Perspectives. *J. Plant Physiol.* **2014**, *171* (9), 656-669.
56. Guinovart, T.; Parrilla, M.; Crespo, G. A.; Rius, F. X.; Andrade, F. J., Potentiometric Sensors Using Cotton Yarns, Carbon Nanotubes and Polymeric Membranes. *Analyst* **2013**, *138* (18), 5208-5215.

CHAPTER 5

SUMMARY AND CONCLUSIONS

In this work, development of an ion selective electrodes functionalized on inkjet printed graphene that was thermally annealing was presented. This project combined the inkjet printing techniques, carbon based nanomaterials, and wearable technology to fabricate a sensor that could help enable the continuous monitoring of patient's sweat potassium concentration.

Inkjet printing technique provides a scalable and cost effective methods to fabricate the graphene electrodes. The thermally annealing process significantly improved the electrical conductivity by 5 orders of magnitude. The sensors functionalized on graphene electrodes with post thermally annealing shows good sensing performance and minimized drift compare to sensors with other carbon based materials. The current electrode fabrication requires post-processing under inert gas environment. To further simplify the fabrication process, Claussen lab is working on replacing thermally annealing process with laser annealing process¹. By applying laser annealing process, the graphene electrodes can be fabricated on flexible substrates that are not suited for high temperature furnace annealing such as polymers, cellulose papers, papers or even fabrics. Since the inkjet printing technology is well-suited for scale manufacturing, an all inkjet printable working electrode and inkjet printable solid state reference electrode could be further developed.

While in this work, the basic characterization of our ISE on IPG electrodes has been conducted, more tests could be done to further understand the sensors' sensing performance. The selectivity tests were conducted to obtain the selectivity coefficient against other ions and test the sensing performance in artificial sweat². However, the proteins in real sweat, the body temperature

fluctuation of human body surface may affect the sensing performance³. Consequently, the sensing performance of the ISE sensor on the human body need to be further tested.

Multiple reasons can cause the sweat potassium level to fluctuate, the potassium sensor can only provide very limited information and ambiguous hint about patients' health status^{4,5}. The further integration of potassium sensors with sensors that can monitor sodium, glucose, lactate, temperature, and pH could help provide real time monitoring of athletes' sports performance⁴, patients physical and psychological stress levels, and/or health status⁶⁻⁷. The data collected by sensors could also be sent to mobile devices such as cellphones for real time data storage and analysis for integration into the wireless technologies with appropriate electronics^{3, 8-9}. The information collected by continuous monitoring could also help provide timely and accurately treatment for patients with chronic disease such as diabetes and hypertension by integrating drug delivery devices to the sensing systems. In conclusion, the inkjet printing technique is a promising method to produce low cost, wearable sensors. The further development of wearable sensors is anticipated to significantly improve people's quality of life.

References

1. Das, S. R.; Nian, Q.; Cargill, A. A.; Hondred, J. A.; Ding, S.; Saei, M.; Cheng, G. J.; Claussen, J. C., 3D Nanostructured Inkjet Printed Graphene via UV-Pulsed Laser Irradiation Enables Paper-Based Electronics and Electrochemical Devices. *Nanoscale* **2016**, *8* (35), 15870-15879.
2. He, Q.; Das, S. R.; Garland, N. T.; Jing, D.; Hondred, J. A.; Cargill, A. A.; Ding, S.; Karunakaran, C.; Claussen, J. C., Enabling Inkjet Printed Graphene for Ion Selective Electrodes with Post-Print Thermal Annealing. *ACS Applied Materials & Interfaces* **2017**.
3. Bandodkar, A. J.; Molinnus, D.; Mirza, O.; Guinovart, T.; Windmiller, J. R.; Valdés-Ramírez, G.; Andrade, F. J.; Schöning, M. J.; Wang, J., Epidermal tattoo potentiometric sodium sensors with wireless signal transduction for continuous non-invasive sweat monitoring. *Biosensors and bioelectronics* **2014**, *54*, 603-609.
4. Holmes, N.; Bates, G.; Zhao, Y.; Sherriff, J.; Miller, V., The Effect of Exercise Intensity on Sweat Rate and Sweat Sodium and Potassium Losses in Trained Endurance Athletes. *Annals of Sports Medicine and Research* **2016**, *3* (2), 1-4.
5. Ďurč, P.; Foret, F.; Pokojová, E.; Homola, L.; Skříčková, J.; Herout, V.; Dastych, M.; Vinohradská, H.; Kubáň, P., New approach for cystic fibrosis diagnosis based on chloride/potassium ratio analyzed in non-invasively obtained skin-wipe sweat samples by capillary electrophoresis with contactless conductometric detection. *Analytical and bioanalytical chemistry* **2017**, *409* (14), 3507-3514.
6. Cazalé, A.; Sant, W.; Ginot, F.; Launay, J.-C.; Savourey, G.; Revol-Cavalier, F.; Lagarde, J.-M.; Henry, D.; Launay, J.; Temple-Boyer, P., Physiological stress monitoring using sodium ion potentiometric microsensors for sweat analysis. *Sensors and Actuators B: Chemical* **2016**, *225*, 1-9.
7. Tang, Y.-M.; Wang, D.-G.; Li, J.; Li, X.-H.; Wang, Q.; Liu, N.; Liu, W.-T.; Li, Y.-X., Relationships between micronutrient losses in sweat and blood pressure among heat-exposed steelworkers. *Industrial health* **2016**, *54* (3), 215-223.
8. Schazmann, B.; Morris, D.; Slater, C.; Beirne, S.; Fay, C.; Reuveny, R.; Moyna, N.; Diamond, D., A wearable electrochemical sensor for the real-time measurement of sweat sodium concentration. *Analytical Methods* **2010**, *2* (4), 342-348.
9. Huang, X.; Liu, Y.; Chen, K.; Shin, W. J.; Lu, C. J.; Kong, G. W.; Patnaik, D.; Lee, S. H.; Cortes, J. F.; Rogers, J. A., Stretchable, wireless sensors and functional substrates for epidermal characterization of sweat. *small* **2014**, *10* (15), 3083-3090.